

THE UNIVERSITY OF CALGARY

Non-reflecting Boundary Condition in Detonation Simulation

by

Yinghua Han

A THESIS

SUBMITTED TO THE FACULTY OF GRADUATE STUDIES
IN PARTIAL FULFILMENT OF THE REQUIREMENTS FOR THE
DEGREE OF MASTER OF SCIENCE

DEPARTMENT OF MECHANICAL AND MANUFACTURING ENGINEERING

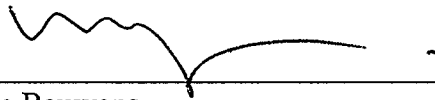
CALGARY, ALBERTA

August, 2003

© Yinghua Han 2003

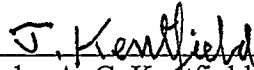
UNIVERSITY OF CALGARY
FACULTY OF GRADUATE STUDIES

The undersigned certify that they have read, and recommend to the Faculty of Graduate Studies for acceptance, a thesis entitled "Non-reflecting Boundary Condition in Detonation Simulation" submitted by Yinghua Han in partial fulfilment of the requirements of the degree of Master of Science.



Supervisor Dr. Luc Bauwens

Department of Mechanical and Manufacturing Engineering



Dr. John A. C. Kentfield

Department of Mechanical and Manufacturing Engineering



Dr. Michael Potter

Department of Electrical and Computer Engineering

Sept. 4, 2003

Date

Detonation is a very rapid and violent form of combustion. A number of important issues associated with occurrence of detonation waves remain poorly understood. Numerical simulation has become one of the main research tools on detonation waves, using Computational Fluid Dynamics (CFD). To limit the computational domain to manageable sizes, it is often useful to perform simulations in a frame of reference attached to the wave. The physical domain is then truncated, resulting in artificial inflow and outflow boundaries. Numerical non-reflecting boundary conditions are then necessary, ensuring that outgoing disturbances do not reflect back into the computational domain. We have implemented effective high order-accurate non-reflecting boundary conditions, coupled with an WENO (weighted essentially non-oscillatory) solver. In this thesis, typical techniques will be introduced on how non-reflecting boundary condition can be implemented. The *characteristic method* which we use will be described in detail. Validation and results for one dimensional shock-tube problem and for two dimensional detonations will be presented.

Acknowledgements

To complete my master degree study after having worked in the aviation industry, and away from university for 14 years, I knew I needed encouragement, hardwork, and a good coach. I was fortunate to have Dr. Luc Bauwens as my supervisor to guide me through the study of detonation simulation in Computational Fluid Dynamics (CFD). I wish to give my special thanks to Dr. Bauwens. At the beginning of my study, he directed me to quickly reach the front line of detonation simulation. His invaluable advice helped me to generate ideas and explore paths in my research. My research with him in non-reflecting boundary conditions for detonation simulation has greatly enriched my academic knowledge in gas dynamics and upgraded my skill in computer programming.

My gratitude also goes to Dr. Doug Philips (University Computing Services) for assisting me with computer programs. He is always ready to respond cheerfully to my questions and to help me troubleshoot.

Lastly, I am grateful to my colleagues for their support: Zhe Liang, Liang Feng, and Daniel Neale Williams.

Table of Contents

Approval Page.....	ii
Abstract.....	iii
Acknowledgements.....	iv
Table of Contents.....	v
List of Tables	vii
List of Figures and Illustrations	viii
List of Symbols, Abbreviations and Nomenclature.....	ix

Chapter 1 Introduction

- 1-1 Detonation
- 1-2 Objectives

Chapter 2 Detonation

- 2-1 History
- 2-2 C-J Theory
- 2-3 ZND Model
- 2-4 Other Steady Detonation Models
- 2-5 Multi-dimensional Structure

Chapter 3 Numerical Simulation of Detonation

- 3-1 Physical Models
 - 3-1-1 Governing Equations
 - 3-1-2 Initial Conditions
 - 3-1-3 Boundary Conditions

3-2 Numerical Issues

3-2-1 Numerical Technique

3-2-2 Monotonicity Preservation

3-2-3 Conservation

3-2-4 CFL Stability Criterion

3-3 WENO Scheme

3-4 Fourth Order Spatial Accuracy Method

3-5 Third Order Accuracy Runge-Kutta Method

3-6 Second Order Accuracy Method

3-7 Implementation

Chapter 4 The Characteristics Method

4-1 Introduction

4-2 Characteristic Form of the One-dimensional Euler Equations

4-3 Riemann Invariants

4-4 Characteristic Form of the Two-dimensional Euler Equations

Chapter 5 Validation

5-1 Pressure Impulse Test

5-2 Shock Tube Test

5-3 Reflection Validation By Relative Error at Shock Waves

5-4 Reflection Validation Using Riemann Variable

5-5 Two-dimensional Validation

Chapter 6 Detonation Cell Size

6-1 Numerically Simulation

6-2 Comparison Between the Two Sets of Results

Chapter 7 Conclusion

List of Tables

Table 3-1.1 The relationship between Z and position in the ZND wave	3.4
Table 3-3.1 Optimal weights C_k^3 ($r = 3$)	3.12
Table 3-3.2 Constant coefficients $a_{k,l}^r$ ($r = 3$)	3.13
Table 5-3.1 Relative errors at the different Mach number	5.8
Table 5-4.1 Riemann variable deviation for different grid sizes (single precision)...	5.12
Table 5-4.2 Riemann variable deviation for different grid sizes (double precision)..	5.14
Table 6-1.1 Parameters	6.1
Table 6-2.1 The Comparison of smoke foils for different domain sizes and BC	6.7

List of Figures and Illustrations

Fig. 2-2.1 Chapman-Jouguet detonation wave	2.5
Fig. 2-2.2 Rayleigh line--Hugoniot curve (C-J)	2.7
Fig. 2-2.3 Rayleigh line--Hugoniot curve (C-J) (Detonation branch)	2.8
Fig. 2-3.1 ZND detonation wave	2.9
Fig. 2-3.2 Rayleigh line--Hugoniot curve (ZND)	2.11
Fig. 2-3.3 Thermodynamic variables profile along x (ZND model).....	2.14
Fig. 2-5.1a Smoked-foil records of propagating detonations	2.16
Fig. 2-5.1b Smoked-foil records of propagating detonations	2.17
Fig. 2-5.2 Propagation of detonation front at time of t_1 and t_2	2.18
Fig. 3-1.1 The chemical reaction progress vs. position in ZND wave	3.4
Fig. 3-1.2 Computational domain and boundaries	3.5
Fig. 3-4.1 Illustration of grid cells	3.13
Fig. 3-7.1 Flowchart of the detonation simulation	3.19
Fig. 5-1.1 Initial pressure profile.....	5.2
Fig. 5-1.2 Pressure and total energy profiles before the disturbance crossing outlet...	5.3
Fig. 5-1.3 Pressure and total energy profiles when the disturbance crossing outlet....	5.3
Fig. 5-1.2 Pressure and total energy profiles after the disturbance crossing outlet.....	5.3
Fig. 5-2.1 Illustration of shock tube solution	5.4

Fig. 5-2.2 Shock tube at time-step 0	5.5
Fig. 5-2.3 Shock tube at time-step 1140	5.6
Fig. 5-2.4 Shock tube at time-step 1500	5.6
Fig. 5-3.1 Relative error vs. Mach number	5.9
Fig. 5-4.1 Riemann variable deviation vs grid size (single precision).....	5.12
Fig. 5-4.2 Riemann variable deviation vs grid size on a log-log scale (single precision).....	5.13
Fig. 5-4.3 Riemann variable deviation vs grid size (double precision).....	5.14
Fig. 5-4.4 Riemann variable deviation vs grid size on a log-log scale (double precision).....	5.15
Fig. 5-4.5 Riemann variable deviation vs grid size on a log-log scale at $x=0.1$ (double precision).....	5.15
Fig. 5-4.6 Riemann variable deviation vs grid size on a log-log scale at $x=0.2$ (double precision).....	5.16
Fig. 5-4.7 Riemann variable deviation vs grid size on a log-log scale at $x=0.3$ (double precision).....	5.16
Fig. 5-4.8 Riemann variable deviation vs grid size on a log-log scale at $x=0.4$ (double precision).....	5.17

Fig. 5-5.1 Smoke foils width: $20 L_{1/2}$, length: $30 L_{1/2}$	5.18
Fig. 5-5.2 Smoke foils width: $20 L_{1/2}$, length: $50 L_{1/2}$	5.18
Fig. 6-1.1 Smoke foil width: $13 L_{1/2}$, length: $30 L_{1/2}$, Non-reflecting BC	6.3
Fig. 6-1.2 Smoke foil width: $13 L_{1/2}$, length: $30 L_{1/2}$, relaxation BC	6.3
Fig. 6-1.3 Smoke foil width: $13 L_{1/2}$, length: $50 L_{1/2}$, relaxation BC	6.3
Fig. 6-1.4 Smoke foil width: $14 L_{1/2}$, length: $30 L_{1/2}$, Non-reflecting BC	6.3
Fig. 6-1.5 Smoke foil width: $14 L_{1/2}$, length: $30 L_{1/2}$, relaxation BC	6.3
Fig. 6-1.6 Smoke foil width: $14 L_{1/2}$, length: $50 L_{1/2}$, relaxation BC	6.4
Fig. 6-1.7 Smoke foil width: $24 L_{1/2}$, length: $30 L_{1/2}$, Non-reflecting BC	6.4
Fig. 6-1.8 Smoke foil width: $24 L_{1/2}$, length: $30 L_{1/2}$, relaxation BC	6.4
Fig. 6-1.9 Smoke foil width: $24 L_{1/2}$, length: $50 L_{1/2}$, relaxation BC	6.4
Fig. 6-1.10 Smoke foil width: $25 L_{1/2}$, length: $30 L_{1/2}$, Non-reflecting BC	6.5
Fig. 6-1.11 Smoke foil width: $25 L_{1/2}$, length: $30 L_{1/2}$, relaxation BC	6.5
Fig. 6-1.12 Smoke foil width: $25 L_{1/2}$, length: $50 L_{1/2}$, relaxation BC	6.5
Fig. 6-1.13 Smoke foil width: $41 L_{1/2}$, length: $30 L_{1/2}$, Non-reflecting BC	6.6
Fig. 6-1.14 Smoke foil width: $41 L_{1/2}$, length: $30 L_{1/2}$, relaxation BC	6.6

Fig. 6-1.15 Smoke foil width: $41 L_{1/2}$, length: $50 L_{1/2}$, relaxation BC 6.6

List of Symbols, Abbreviations and Nomenclature

a	Acceleration
A	$n \times n$ matrix
b	Arbitrary constant
B	$n \times n$ matrix
c	Speed of sound, arbitrary constant
c_p	Specific heat at constant pressure
c_v	Specific heat at constant volume
C	Arbitrary constant
D	Detonation velocity
D_{C-J}	Chapman-Jouguet detonation velocity
E	Total energy per unit volume
E_0	Activation energy
f	Overdrive factor
F	Vector fluxes in the x direction
G	Vector of fluxes in the y direction
h	Enthalpy
K	Rate multiplier
L	Length
$L_{1/2}$	Half-reaction length
M	Mach number
M_{C-J}	C-J Mach number

m	Mass flow rate, Riemann variable
p	Pressure
$q(x)$	Chemical heat release
Q	Total chemical heat release
R	Pressure ratio
s	Entropy
t	Time
$t_{1/2}$	Half-reaction time
T	Temperature
u	Velocity
u_x	Velocity in x direction
u_y	Velocity in y direction
U	Primitive vector
\tilde{U}	Vector of conserved variables
v	Specific volume
V	Vector of characteristics variables
w	Angular velocity
Z	Mass fraction reactant
α	Arbitrary factor
γ	Ratio of specific heats
λ	Extent of chemical reaction, eigenvalues of A
μ	Eigenvalues of B
ν	FCT diffusion coefficient

ρ	Density
φ	Slope
τ	Relaxation factor
Ω	Arbitrary volume

Symbols

Δ	Step size
\sim	Indication of dimensional variable or conservative variable
\wedge	Indication of numerical variable
∇	Indication of derivative
\rightarrow	Indication of vector

Subscripts

0	Pre-shock conditions or initial conditions
1	Conditions at the end of the reaction zone
C-J	Chapman-Jouget conditions
i	Cell index in x direction
j	Cell index in y direction
k	Cell index in z direction
t	Derivative with respect to t
x	Derivative with respect to x
y	Derivative with respect to y

Superscripts

0	Values for old time step
n	Time index

INTRODUCTION

1-1 Detonation

Detonation is the most rapid and violent form of combustion. Detonation waves can be described as an interaction between diffusionless gas dynamics and chemistry. Diffusive mechanism such as heat conduction and mass diffusion, which are very important in flames, can be neglected. In detonations, all important energy transfer involves chemistry and strongly compressible flow. The material is consumed 10^3 to 10^8 times faster than if in a flame (Fickett & Davis 1979), and the rate of energy conversion is thus extremely high. For example, a detonation wave with an area of 20 square meters releases power at a rate equivalent to all the power that the earth receives from the sun. This property makes detonation either very dangerous or very useful.

The detonation phenomenon was first recognized in 1881. The first attempt to theoretically explain the phenomenon is the well-known Chapman-Jouguet theory. It assumes that the entire flow is one-dimensional, and the front is treated as a

discontinuity plane at which heat is released. The resulting Rankine-Hugoniot conservation laws apply across the discontinuity, where the chemical reaction is considered to complete instantaneously. Based on these assumptions, it is found that a minimum value exists for detonation velocity, or a maximum value for deflagration velocity, which are called the upper and lower Chapman-Jouguet (C-J) limits respectively. There is no solution for the wave speed when the detonation velocity is lower than the upper C-J limit or the deflagration velocity is higher than the lower C-J limit. This simple theory works reasonably well for predicting detonation velocities in gases.

In 1927, the spinning detonation phenomenon was discovered, providing an early indication that real detonations might be more complex than the planar model. Meanwhile, recognizing the finite nature of reaction rates, Zel'dovich (1940), von Neumann (1942) and Döring (1943) independently proposed the model now named with their initials, ZND. The ZND model also assumes that the flow is steady and one-dimensional. It still describes the leading shock as a singularity, but resolves finite rate chemistry behind the shock. However, mounting evidence was indicating that actual detonations were unsteady, and that the leading shock was not planar.

In the past few decades, researchers have been trying to better understand the phenomena of detonation in order to prevent uncontrolled detonation or even use it to design advanced propulsion systems such as the Pulse Detonation Engine (PDE) and the Pulse Detonation Rocket Engine (PDRE). A number of important issues associated with occurrence of detonation waves remain poorly understood, such as deflagration-to-detonation transition, which is the main mechanism leading to detonation. Some issues, such as the stability and the structure of detonations, have been extensively studied in experiments and numerical simulations and they are better understood.

With the advent of Computational Fluid Dynamics (CFD), numerical simulation of shocks and detonation waves has become feasible. Multi-dimensional detonation

structures observed in experiments can be predicted and analyzed by numerical simulation. Two-dimensional transverse wave structures with single step chemistry have been simulated (Taki and Fujiwara 1978/1981, Oran et al. 1981/1982, Bourlioux 1992, Williams & Bauwens 1995, and Bauwens & Williams 1996). Because computational domains are unavoidably finite, large or infinite physical domains need to be truncated, resulting in artificial boundaries. The non-reflecting numerical boundary condition (BC) is a useful artificial boundary condition ensuring that outgoing disturbances will not be reflected back into the computational domain. The non-reflecting BC is not a true representation of an infinite domain, but in most cases, it will provide a better approximation than other models, which by their very nature, will result in strong reflections.

1-2 Objectives

The objective of this research is to investigate available methods of non-reflecting boundary condition, select the most appropriate one for incorporation in our high accuracy detonation code and to implement and test it. Listed below are the specific objectives for this research:

- Investigate numerical simulation algorithms used within the computational domain for time and spatial derivatives and develop a high order accuracy algorithm for spatial derivatives used at boundary condition.
- Implement the selected method into our program with high order accuracy.
- Validate the reflection at an outflow boundary.

This thesis is organized as follows: Chapter 2 contains a review of the history of detonation simulation and classical models, such as the C-J theory as well as the ZND

model. Next, numerical issues related to our simulations are reviewed in Chapter 3. The scheme used for the inner computational domain and at the boundaries is described in Chapter 3. Different methods for non-reflecting boundary conditions are described briefly and the characteristics method, which is the method selected here, is introduced in detail in Chapter 4. Chapter 5 concentrates on validation of the characteristics method and analysis of the reflection in one-dimensional flow. Chapter 6 shows results from application of the characteristics based non-reflecting method in two-dimensional detonation simulations. Finally, Chapter 7 includes a summary and the conclusions.

DETONATION

2-1 History

In early times, the word detonation was used when referring to the sudden decomposition of certain chemicals and mixtures with the production of considerable noise, “like thunder.” Nowadays, in combustion science, the term detonation specifically describes shock-induced combustion (Strehlow 1984). The leading part of the detonation front is a strong shock wave propagating into the explosive or unreacted mixture. This shock heats the material by compressing it, thus dramatically increasing temperature-sensitive chemical reaction rates. Finally, the rapid reaction that ensues results in expansion of the fluid, which supports the shock wave.

The detonation phenomenon was first observed by Berthelot and Vieille and Mallard and LeChatelier in 1881 independently. Chapman (1899) and Jouguet (1905) developed a simple one-dimensional theory which explained the phenomenon theoretically. The Chapman-Jouguet theory assumes that concentrated heat release is

associated with a gas dynamic discontinuity across which the conservation laws are thus reduced to a set of jump conditions called the Rankine-Hugoniot conditions. Their theory made it possible to predict detonation velocities in gases. It provided a strong framework for classification of combustion waves into two distinct families, namely, supersonic shock-supported detonations and subsonic shockless deflagrations. The theory is discussed in more detail in the following section.

In 1927, Campbell and Woodhead discovered the phenomenon of spinning detonation, which indicated that real detonations might be more complicated than the C-J model. A significant improvement to the C-J theory was made independently by Zeldovich (1940) in Russia, von Neumann (1942) in the United States, and Döring (1943) in Germany. Their model has come to be called the ZND model of detonation. It is based on the Euler equations of hydrodynamics and still assumes that the flow is one-dimensional and steady. In addition, the shock is still treated as a discontinuity. But unlike the C-J model, the ZND model resolves the reaction zone for arbitrary finite rate models.

During the period of 1950-1963, many researchers including Berets, Greene, and Kistiakowsky, tried to compare one-dimensional theory with experimental measurements in gaseous systems. Their results suggested that the effective state point at the end of the reaction zone was in the vicinity of the weak detonation branch of the Hugoniot line. Instead of C-J (sonic) point as the theory would predict, the measured pressures and densities are typically ten to fifteen percent lower than the calculated values by C-J theory and the flow is supersonic instead of sonic.

This disagreement between experiments and theory forced researchers to consider detonations: 1) in which the chemical reaction contains an arbitrary number of equilibrium chemical reactions so that a state of global chemical equilibrium can be attained; or 2) is described by the Navier-Stokes equations, including heat conduction,

diffusion, and viscosity, but with a single forward chemical reaction; or 3) in which the flow is slightly two-dimensional and affected by boundary layers or edge effects. In each of these cases, the flow equations are reduced to a set of autonomous, first-order, ordinary, differential equations with the detonation velocity as a parameter. However, without drastic and unwarranted assumptions to simplify the equations, analytical solutions cannot be obtained.

Because significant three-dimensional features were observed in experiments, instead of pursuing one-dimensional weak solutions, efforts were also directed toward studying detonation stability and the structure of the detonation front. The structure of detonation waves has been studied extensively for more than sixteen years and the now generally accepted three-dimensional model has been established mainly based on soot patterns formed on detonation tube walls. A three-dimensional structure has also been proposed, especially for single spin detonation in a round tube and multi-head detonation in a rectangular tube. These will be discussed in detail in section 2-5.

2-2 C-J Theory:

If diffusive phenomena, which include viscosity, heat conduction and mass diffusion, are neglected, the flow can be expressed by the reactive Euler equations:

$$\left\{ \begin{array}{l} \frac{\partial \rho}{\partial t} + \bar{\nabla} \cdot (\rho \bar{u}) = 0 \\ \frac{\partial (\rho \bar{v})}{\partial t} + \bar{\nabla} \cdot (\rho \bar{u} \otimes \bar{u} + p \bar{I}) = 0 \\ \frac{\partial E}{\partial t} + \bar{\nabla} \cdot (\rho Z \bar{u}) = -K \rho Z e^{-\left(\frac{E_0}{p/\rho}\right)} \\ \frac{\partial (\rho s)}{\partial t} + \bar{\nabla} \cdot (\rho s \bar{u}) \geq 0 \end{array} \right. \quad (2-2.1)$$

Where: $E = \frac{p}{\gamma - 1} + Q \rho Z + \frac{1}{2} \rho \bar{u} \cdot \bar{u}$

$$\bar{u} = u_x \bar{i} + u_y \bar{j} + u_z \bar{k};$$

$$\bar{\nabla} = \bar{i} \frac{\partial}{\partial x} + \bar{j} \frac{\partial}{\partial y} + \bar{k} \frac{\partial}{\partial z};$$

$$p \bar{I} = \bar{i} p_x + \bar{j} p_y + \bar{k} p_z$$

The basic assumptions leading to the C-J model are that the entire flow is steady and one-dimensional, hence isentropic except at the discontinuity, and that the shock and reaction zone collapse into a single jump discontinuity in which complete reaction takes place. The reaction can then be treated as a simple heat addition Q . The resulting model is shown in Fig. 2-2.1.

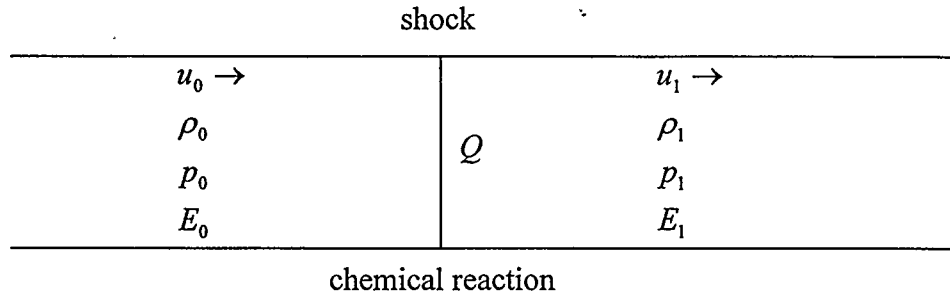


Fig. 2-2.1 Chapman-Jouguet detonation wave

Based on these assumptions, the Euler equations, Eqs. (2-2.1), are reduced to the following jump conditions across the reactive shock, known as the Rankine-Hugoniot conditions:

$$\left\{ \begin{array}{l} \rho_0 u_0 = \rho_1 u_1 = m \\ p_0 + \rho_0 u_0^2 = p_1 + \rho_1 u_1^2 \\ h_0 + \frac{1}{2} u_0^2 + Q = h_1 + \frac{1}{2} u_1^2 \end{array} \right. \quad (2-2.2)$$

where: $h = \frac{\gamma}{(\gamma-1)} \frac{p}{\rho}$

Eliminating u_0 and u_1 and combining conservation of mass and momentum, one obtains the Rayleigh line, Eq. (2-2.3). Combining conservation of mass, momentum, and energy, and eliminating u_0 , u_1 , h_0 , and h_1 in favor of pressure p and density ρ , the Hugoniot curve, Eq. (2-2.4), can be obtained. (The Hugoniot curve does rely upon mass conservation, but it is independent of the specific value of the mass flow rate across the discontinuity.)

$$\text{Rayleigh line: } \frac{p_1}{p_0} - 1 = -\frac{m^2}{\rho_0 p_0} \left(\frac{\rho_0}{\rho_1} - 1 \right) \quad (2-2.3)$$

$$\text{Hugoniot curve: } \frac{p_1}{p_0} = \frac{[2Q + (\gamma + 1)/(\gamma - 1)] - \rho_0 / \rho_1}{[(\gamma + 1)/(\gamma - 1)](\rho_0 / \rho_1) - 1} \quad (2-2.4)$$

These two lines, plotted in the p_1 / p_0 vs. ρ_0 / ρ_1 ($=v_1 / v_0$) plane, are shown in Fig. (2-2.2). The Rayleigh line is a straight line, while the Hugoniot curve is a hyperbola. Starting from the unshocked state $p_1 / p_0 = 1$, $v_1 / v_0 = \rho_0 / \rho_1 = 1$, actual solutions (i.e. combustion waves) correspond to intersection points between the Rayleigh and Hugoniot lines. Furthermore, from Eq. (2-2.3), it is clear that the slope of the Rayleigh line is negative in all cases, and one can see on the figure that there is a range of slopes for the Rayleigh line (hence mass flow rate) for which intersections do not exist. This range of slopes is comprised between two values at which tangency occurs between the two lines, at two points that have come to be known as the lower and the upper Chapman-Jouguet (C-J) points. Reaction with increasing pressure and density are detonation waves. Reaction with decreasing pressure and density are called deflagrations.

The conservation conditions require that the final state point in the p_1 / p_0 , v_1 / v_0 plane must belong to both the Rayleigh line and the Hugoniot curve. If the slope of Rayleigh line is too slight on the detonation branch or too steep on the deflagration branch, there will be no intersection of the Rayleigh lines and the Hugoniot curve. So, there are minimum slope (ϕ_{\min}) on the detonation branch and maximum slope (ϕ_{\max}) on the deflagration branch, corresponding to the tangent points of the Rayleigh lines and Hugoniot curve, called the upper C-J point and lower C-J point respectively. If $\phi > \phi_{\min}$ on the detonation branch or $\phi < \phi_{\max}$ on the deflagration branch, then there will be two intersections, called the strong solution and weak solution respectively. The current study will focus on detonation, which is the main objective.

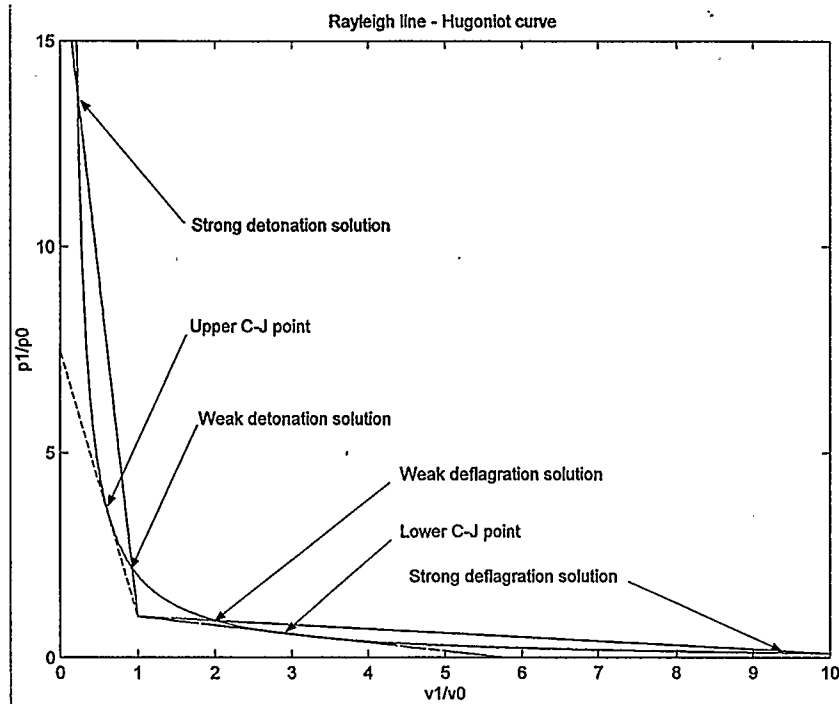


Fig. 2-2.2 Rayleigh line--Hugoniot curve (C-J)

Combining the Rayleigh line and Hugoniot curve, the tangent point data can be obtained. The C-J detonation velocity, i.e. the minimum velocity of a detonation wave, can then be derived:

$$D_{C-J} = \sqrt{\gamma} \left(\sqrt{1 + \frac{Q(\gamma^2 - 1)}{2\gamma}} + \sqrt{\frac{Q(\gamma^2 - 1)}{2\gamma}} \right)$$

The Rayleigh line contains the factor m ($= \rho_0 u_0 = \rho_0 D$), which is proportional to the detonation velocity. For a velocity below C-J velocity, there is no intersection between the Rayleigh line and the Hugoniot curve, so there is no solution that satisfies all conservation laws. For a velocity above C-J velocity, the Rayleigh line and the Hugoniot curve have two intersections, named strong detonation solution (S) and weak detonation solution (W). See Fig. 2-2.3. The weak solution is rejected because there is no shock for the weak solution path; and this is inconsistent with the postulated condition, which is

that detonation is shock-induced combustion.

Detonations with velocity greater than the C-J velocity are known as overdriven detonations. The overdrive factor f is defined as $f = \left(\frac{D}{D_{C-J}} \right)^2$.

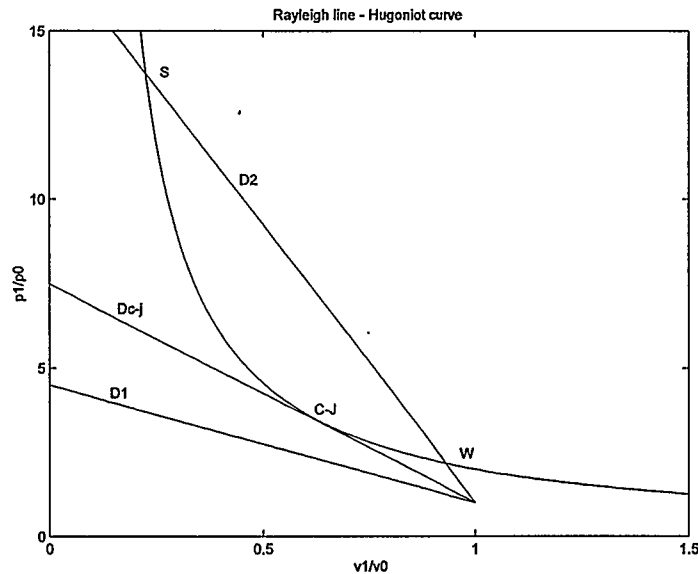


Fig. 2-2.3 Rayleigh line--Hugoniot curve (C-J) (detonation branch)

2-3 ZND Model

Although C-J theory successfully predicts the velocity of freely propagating detonations, it does not describe the internal wave structure. Zel'dovich (1940), von Neumann (1942), and Döring (1943) independently developed the one-dimensional theory for the internal structure of a detonation. Like the C-J theory, their ZND model is based upon the assumptions that the flow is steady and one-dimensional. All diffusive mechanisms are neglected, but now the chemical reaction rate while still zero in front of shock is resolved behind the shock, according to some prescribed finite rate models. Fig. (2-3.1).

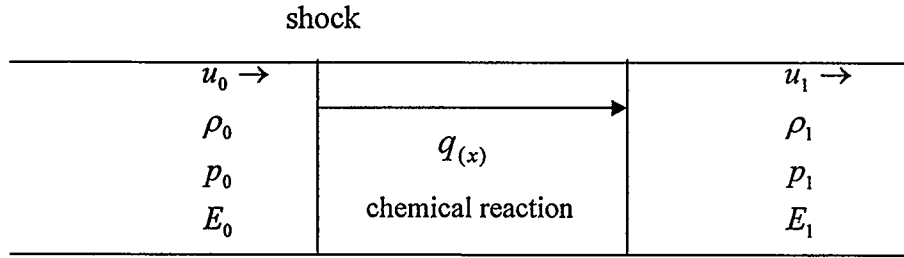


Fig. 2-3.1 ZND detonation wave

Under these assumptions, the steady Euler equations result in Eqs. (2-3.1). The mass and momentum equations are the same as those for the jump discontinuity, Eqs. (2-2.2) and Eqs. (2-3.1). So the Rayleigh lines described in Eqs. (2-2.3) and (2-3.2) are the same in the ZND model as they were in the C-J model. However, the energy or Hugoniot equation for the ZND model is a function of the longitudinal position x . In particular, $q = q(x)$ is the total heat release from the shock to x . Alternatively, a progress variable $\lambda(x)$ is introduced. $\lambda(x)$ is the extent of chemical reaction, measured as the fraction of the total heat release which varies continuously from 0 to 1. For typical multi-step and multi-species kinetic model, $\lambda(x)$ is implicitly determined by the set of rate equations, of the form $\frac{dZ_i}{dx} = f_i(Z_1, \dots, Z_n)$. Integration of this usually stiff system, coupled with mass and momentum, becomes necessary.

$$\left\{ \begin{array}{l} \rho_0 u_0 = \rho_1 u_1 = m \\ p_0 + \rho_0 u_0^2 = p_1 + \rho_1 u_1^2 \\ h_0 + \frac{1}{2} u_0^2 + q = h_1 + \frac{1}{2} u_1^2 \\ q = Q \lambda(x) \end{array} \right. \quad (2-3.1)$$

The Rayleigh line is independent of the heat release. The only difference is that instead of a constant heat release Q , heat release q varies along x , and different, partial reaction, Hugoniot lines can be constructed for any special value of $q(x)$. Thus, a series of Hugoniot curves similar to those obtained in section 2-2 can be introduced for arbitrary values of partial heat release $q(x)$, or $\lambda(x)$.

$$\text{Rayleigh line: } \frac{p_1}{p_0} - 1 = -\frac{m^2}{\rho_0 p_0} \left(\frac{\rho_0}{\rho} - 1 \right) \quad (2-3.2)$$

$$\text{Hugoniot curve: } \frac{p_1}{p_0} = \frac{[2q + (\gamma + 1)/(\gamma - 1)] - \rho_0 / \rho}{[(\gamma + 1)/(\gamma - 1)](\rho_0 / \rho) - 1} \quad (2-3.3)$$

$$\text{Where: } m = u_0 \rho_0 = u_1 \rho_1 = \sqrt{f} M_{C-J} c_0 \rho_0$$

Taking $\gamma = 1.2$, $f = 1.2$, $Q = 50$, the $p_1 / p_0 - v_1 / v_0 (= \rho_0 / \rho_1)$ diagram is presented in Fig. 2-3.2. The Hugoniot curve with $\lambda = 1$ is the complete reaction curve. From C-J theory, for any particular value of the detonation velocity $D (> D_{C-J})$, there are either two solutions, called the strong (S) and weak (W) solutions respectively or only one double solution (C-J) to the two conditions (Hugoniot curve and Rayleigh line), if the Rayleigh line is tangent to the Hugoniot curve. Finally, for lower D , there is no solution. One can also show that, along the Hugoniot curve, entropy is maximum at the upper C-J point, and minimum at the lower C-J point. It can be shown that the flow at the upper or strong point is subsonic and supersonic at the weak point. At the tangent point, the flow is sonic.

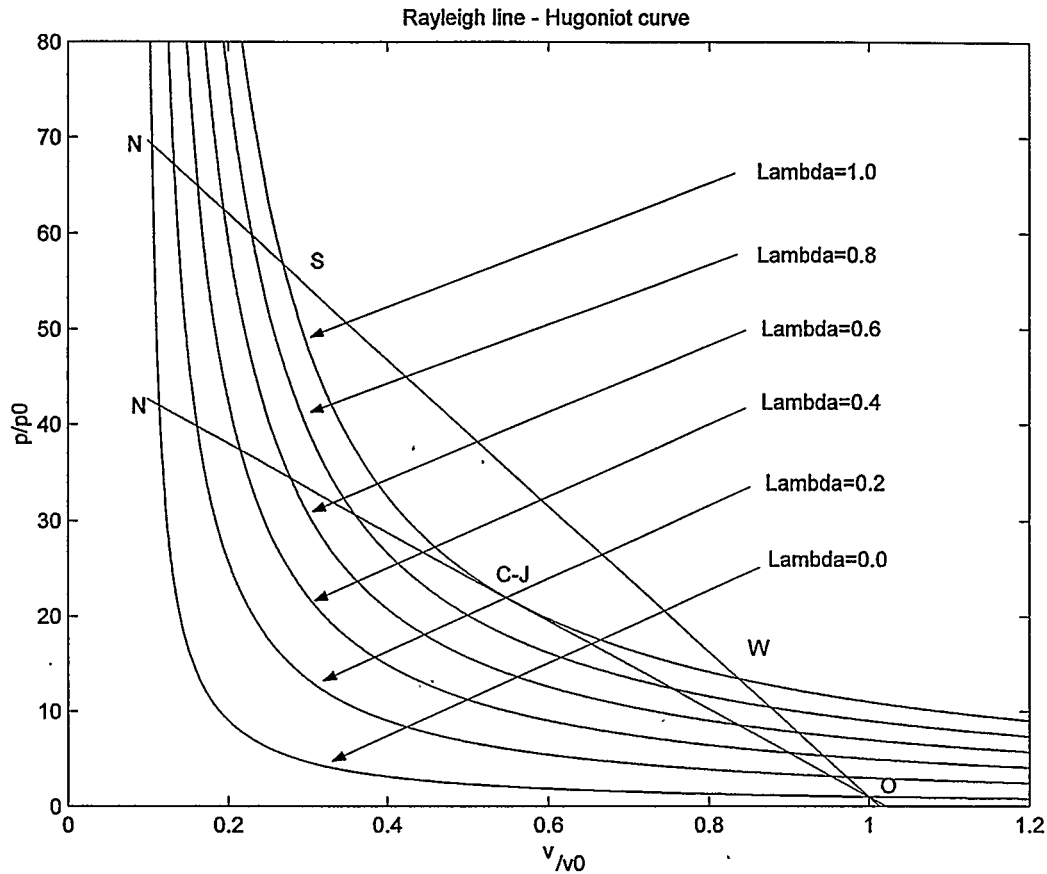


Fig. 2-3.2 Rayleigh line--Hugoniot curve (ZND)

The ZND model resolves spatial heat release. Its description on the Hugoniot diagram requires a complete process starting at the initial unburnt state and ending on the burnt Hugoniot curve. For the weak solution, one can go directly from O to W smoothly. But the strong solution requires a shock, since point S can only be reached from above as shown on the Fig. 2-3.2.

In this model, then as a particle passes through the shock at the front, the state is first changed instantaneously, without reaction, from the initial point O to the von Neumann point N, which corresponds to crossing the leading shock. It then moves down the Rayleigh line, from N to S, as the reaction proceeds. The final state of the reaction zone can be either a strong point S or the C-J point. The only conceivable path to the

weak final point would correspond to a weak smooth (shockless) wave OW. It is conceivable that these might exist briefly in transient processes, but in theoretical scenarios that rely on them, the ultimate solution is always a strong C-J wave (Short, et al. Bauwens, 2000, 2002).

Next, the evolution of the thermodynamic variables in the reaction zone is obtained. For a given overdrive factor f , the thermodynamic variables at the von Neumann point can be obtained, Fig. 2-3.2. The detonation velocity is:

$$D = \sqrt{f} D_{C-J} = \sqrt{f\gamma} \left(\sqrt{1 + \frac{Q(\gamma^2 - 1)}{2\gamma}} + \sqrt{\frac{Q(\gamma^2 - 1)}{2\gamma}} \right)$$

From the conservation laws, Eq. (2-3.1), one can obtain all thermodynamic variables for a given λ , the extent of chemical reaction (for instance, Lee and Stewart 1990).

$$\frac{p}{p_s} = a + (1-a) \sqrt{1 - \frac{b\rho_s Q\lambda}{p_s}}, \quad \frac{u}{c_s} = \frac{(1-p/p_s)}{\gamma M_s} + M_s, \quad \frac{\rho}{\rho_s} = \frac{c_s M_s}{u}$$

$$M_s^2 = \frac{(\gamma-1)M^2 + 2}{2\gamma M^2 - (\gamma-1)}, \quad a = \frac{\gamma M_s^2 + 1}{\gamma + 1}, \quad b = \frac{2\gamma M_s^2(\gamma-1)}{(1-a)^2(\gamma+1)}$$

In addition to the conservation laws, a single step chemical reaction model is used, i.e., along a Lagrangian particle path:

$$\frac{d\lambda}{dt} = r(p, T, \lambda) \quad (2-3.4)$$

For instance, the simple first-order Arrhenius form for the reaction rate is:

$$\frac{d\lambda}{dt} = K(1-\lambda)^{\nu} e^{-\frac{E_0}{pT\rho}} \quad (2-3.5)$$

Considering that particles travel at speed u , Eq. (2-3.5) is equivalent to Eq. (2-3.6):

$$u \frac{d\lambda}{dx} = K(1-\lambda)^{\nu} e^{-\frac{E_0}{pT\rho}} \quad (2-3.6)$$

Where K is the rate multiplier, which serves only to set the time and length scales. Using the time (or length) from the shock to the point where half the heat has been released corresponds to setting a value of K such that $t_{1/2} = 1$ (or $L_{1/2} = 1$) when $\lambda = \frac{1}{2}$ (for the reaction order $\nu \geq 1$, the length to complete reaction approaches infinity; the full reaction length is thus not useful). Hence, one can obtain Eq. (2-3.7) [or Eq. (2-3.8)] by integrating Eq. (2-3.5) [or Eq. (2-3.6)]:

$$K = \int_0^{0.5} \frac{e^{-\frac{E_0}{pT\rho}}}{(1-\lambda)^{\nu}} d\lambda, \quad \text{for } t_{1/2} = 1 \quad (2-3.7)$$

$$K = \int_0^{0.5} \frac{ue^{-\frac{E_0}{pT\rho}}}{(1-\lambda)^{\nu}} d\lambda, \quad \text{for } L_{1/2} = 1 \quad (2-3.8)$$

After the rate multiplier K is obtained, rearranging Eq. (2-3.6), one can obtain a relationship between the position x and the extent of chemical reaction λ , Eq. (2-3.9).

$$x = \frac{1}{K_0} \int_0^\lambda \frac{ue^{\frac{E_0}{P/\rho}}}{(1-\lambda)^\nu} d\lambda \quad (2-3.9)$$

Taking $\nu = 0.999$, then pressure, temperature, the extent of chemical reaction, and velocity profiles along x for a one-dimensional ZND wave can all be found. They are plotted in Fig. 2-3.3.

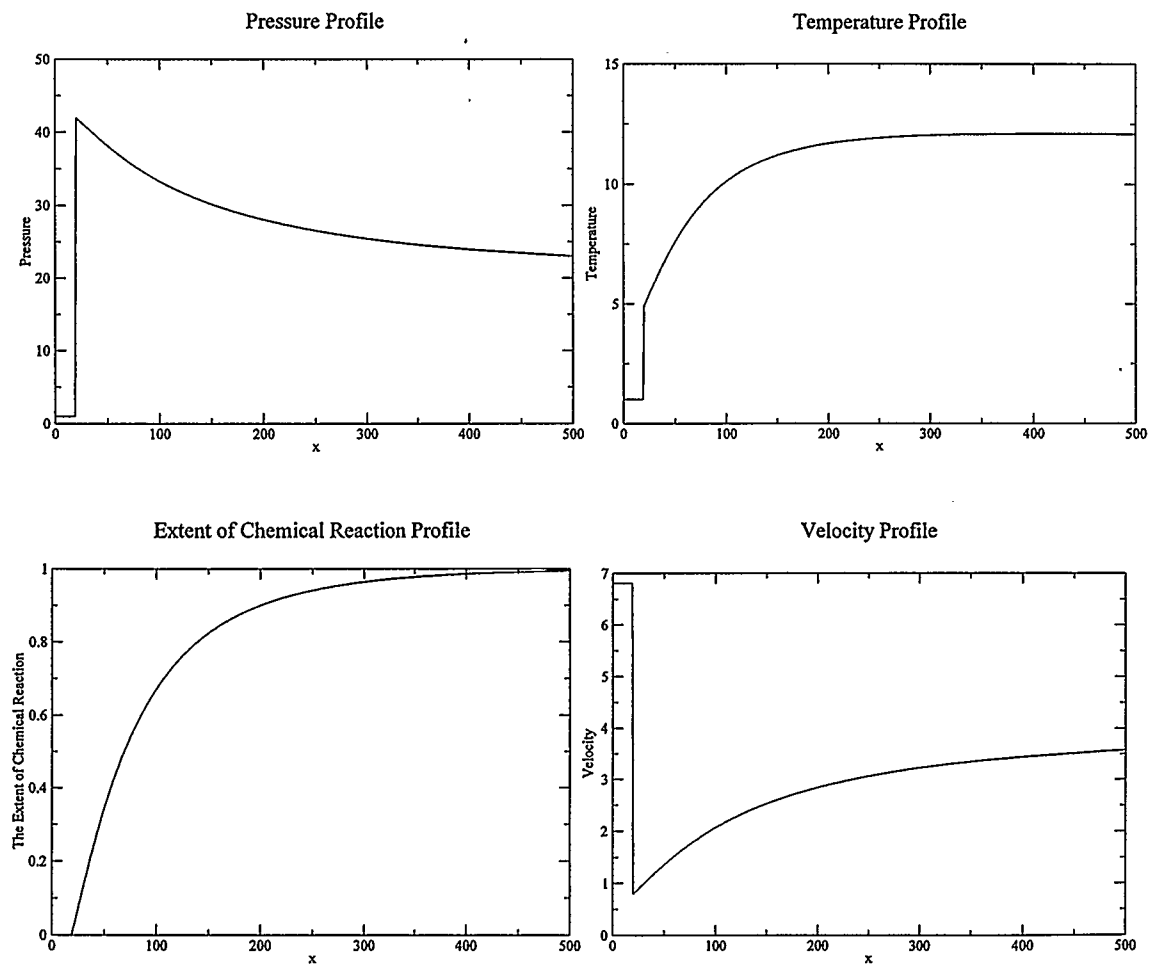


Fig. 2-3.3 Thermodynamic variables profile along x (ZND model)

2-4 Other Steady Detonation Models

In section 2-3, the ZND model of steady detonation was constructed. As mentioned in the introduction, there are disagreements between experiments and theory. Typical measured pressure and densities are ten to fifteen percent below the calculated C-J values, and the detonation velocities are one half to one percent above. These disagreements forced researchers to look for other types of steady solutions.

By removing some of the restrictions of the ZND model, other types of steady solutions can be obtained, such as eigenvalue detonations (Fickett & Davis 1979). The eigenvalue solution is fairly close to experimental results. For a slight radial divergence of the flow, or viscosity, pathological detonations may exist if the reaction includes a decrement in the number of moles or if the chemical reaction ends with an endothermic step. In the eigenvalue solution, the location of the final state on the Hugoniot curve of detonation and the steady propagation velocity depend on the constitutive details.

2-5 Multi-dimensional Structure

The one-dimensional planar detonation structure revealed by the models described above is useful, but more in-depth experiments indicate that real detonations are more complex. For instance, the spin phenomenon, discovered by Campbell and Woodhead in 1927, showed disagreement between experiments and the ZND model. Denisov and Troshin (1959), and White (1961), noticed that detonations were unsteady and exhibited a three-dimensional structure which extended from the leading shock until far back into the reaction zone. This structure is characterized by a non-planar leading shock wave with many shock sections convex toward the incoming flow.

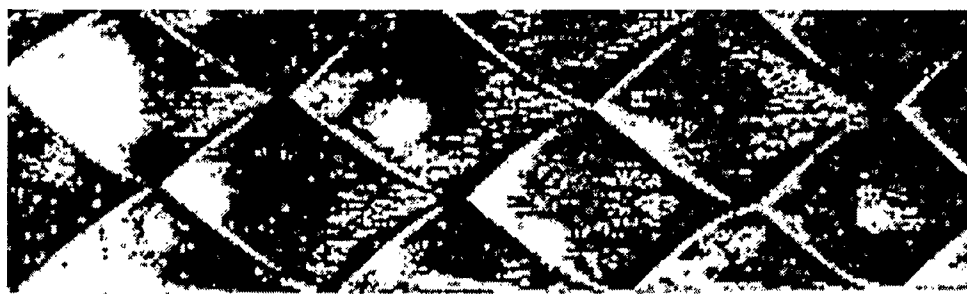
A widely used technique to observe detonation structure is Schlieren photography.

This technique was first applied by Denisov and Troshin in 1959. Following that, a number of researchers, including Schott (1965), Soloukhin (1965), Edwards et al. (1970), Strehlow et al. (1967), Moen et al. (1985) and Shepherd et al. (1986), successfully used the smoke foil technique to unveil the detonation structure. In this technique, foil covered with soot is placed on the walls of a detonation or shock tube. A few examples of smoke-foil records with propagating detonation are shown in Fig. 2-5.1 (Strehlow 1984).



a

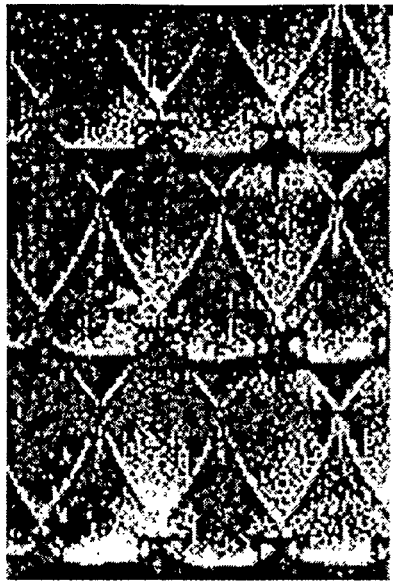
(a) Rectangular mode, showing side, top and end foil records; $2 \text{ H}_2 + \text{O}_2 + 3 \text{ Ar}$, $P_0 = 14 \text{ kPa}$, entire record shown.



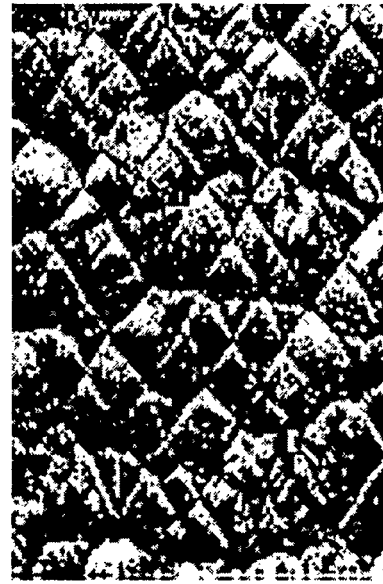
b

(b) Planar mode; $0.2 \text{ H}_2 + 0.1 \text{ O}_2 + 0.7 \text{ Ar}$, $P_0 = 9.3 \text{ kPa}$, entire record shown.

Fig. 2-5.1a Smoke-foil records of propagating detonations



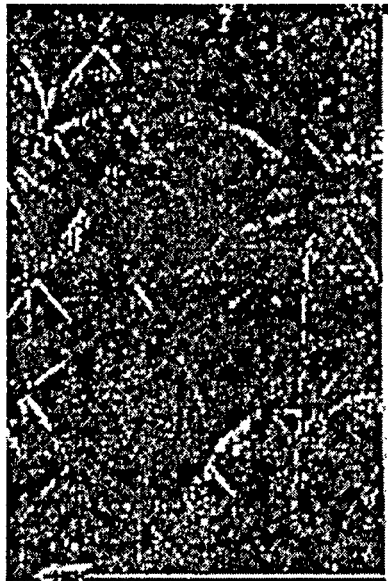
c



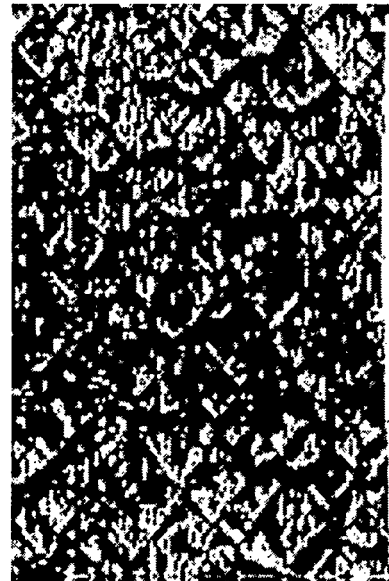
d

(c) Very regular structure; $0.0625 \text{ C}_2\text{H}_4 + 0.1875 \text{ O}_2 + 0.75 \text{ Ar}$, $P_0 = 13.33 \text{ kPa}$

(d) Relatively regular structure; Acetylene-oxygen, $\Phi = 0.625$, $P_0 = 6.67 \text{ kPa}$.



e



f

(e) Irregular structure; $2 \text{ H}_2 + \text{O}_2$, $P_0 = 16 \text{ kPa}$.

(f) Irregular structure; $0.25 \text{ H}_4 + 0.75 \text{ O}_2$, $P_0 = 5.33 \text{ kPa}$.

Fig. 2-5.1b Smoke-foil records of propagating detonations

These experimental photographs reveal a diamond pattern of detonation structures, called cells. The cell is formed by the track of triple points on the smoke foil, which is the intersection of incident shock, reflected shock, and Mach stem. Fig. 2-5.2 depicts a typical propagating Mach stem on a detonation front at two times, t_1 and t_2 . Here, IS, MS, RS, SS, and T stand for incident shock, Mach stem, reflected shock, slip stream, and triple point respectively. Each shock propagates in the direction normal to itself. As time progresses, the triple point is essentially generating both Mach-stem and reflected shocks and overriding the incident shock.

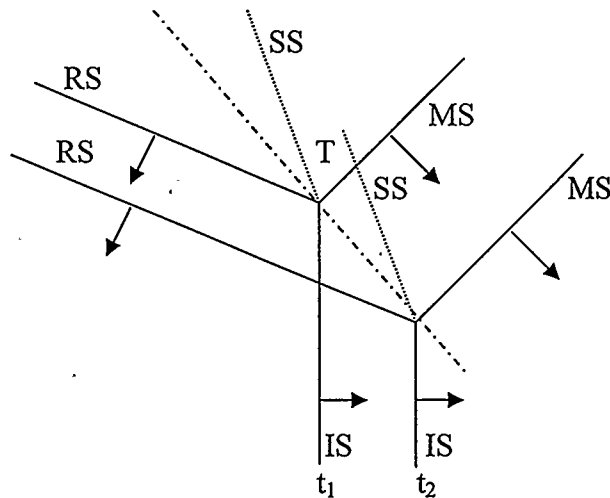


Fig. 2-5.2 Propagation of detonation front at time of t_1 and t_2

With the development of Computational Fluid Dynamics, numerical simulation of shocks and detonation structure has become commonplace. Taki & Fujiwara (1978, 1981) and Oran et al. (1981, 1982) performed early simulations of gaseous detonation, which clearly showed the transverse wave structure. The structure of detonation simulation will be discussed in more detail in Chapter 6.

In the past two decades, the structure of detonation has been studied extensively

in experiments and numerical simulations. All these studies show that an interior shock joins to the leading shock in the conventional three-shock configuration. The Mach stem and the incident shock are part of the leading shock and the transverse wave is the reflected shock.

Triple points and transverse waves move sideways across the front. Groups of them moving in the same direction take up a preferred spacing on the order of 100 reaction-zone lengths. They are not steady, but continually decaying, and only stay alive by periodic rejuvenation through collision with other transverse waves moving in the opposite direction (Fickett & Davis 1979).

Our work is based on the theories discussed above. We study the detonation structures by numerical techniques. The numerical issues and the schemes used in our simulations will be discussed in the following chapter.

NUMERICAL SIMULATION OF DETONATION

This chapter deals with the main issues in numerical simulation of multi-dimensional detonations. Section 3-1 presents the physical model. In sections 3-2 to 3-6, the numerical schemes used in this study are introduced, although the method developed for dealing with non-reflecting boundary conditions at exits is dealt with in a separate chapter, Chapter 4.

3-1 Physical Models

3-1-1 Governing Equations

In this study, the fluid is assumed to be an ideal gas with constant specific heats. Viscous, thermal and mass diffusion are neglected. Chemistry is modeled assuming no change in the number of moles and single step reaction (from reactants to products) with an Arrhenius depletion rate. Under these assumptions, the reactive two-dimensional Euler Equations, Eqs. (2-2.1), can be written in vector form as:

NUMERICAL SIMULATION OF DETONATION 3.2

$$\frac{\partial \tilde{U}}{\partial t} + \frac{\partial \tilde{F}}{\partial x} + \frac{\partial \tilde{G}}{\partial y} + \tilde{S} = 0 \quad (3-1.1)$$

All variables have been made dimensionless with respect to the inflow state, $\tilde{\rho}_0$, \tilde{p}_0 , and length has been scaled by the half-reaction length $L_{1/2}$ (or half-reaction time $t_{1/2}$) of the ZND wave. For a rate law with order ≥ 1 , the length to complete reaction is infinite; for the sake of generality, $L_{1/2}$, a scale that always exist regardless of the data, is used. Thus, the dimensionless variables are:

$$\rho = \tilde{\rho} / \tilde{\rho}_0, \quad p = \tilde{p} / \tilde{p}_0, \quad T = \frac{\tilde{T}}{\tilde{p}_0 / (R \tilde{\rho}_0)},$$

$$u_x = \tilde{u}_x / \tilde{u}_0 = \tilde{u}_x / \sqrt{\tilde{p}_0 / \tilde{\rho}_0}, \quad u_y = \tilde{u}_y / \tilde{u}_0 = \tilde{u}_y / \sqrt{\tilde{p}_0 / \tilde{\rho}_0}$$

$$x = \tilde{x} / L_{1/2}, \quad y = \tilde{y} / L_{1/2}, \quad t = \tilde{t} / t_{1/2},$$

Using the dimensionless variables, the reactive two-dimensional Euler equations, Eqs. (3-1.1), can be written in the dimensionless form as:

$$\frac{\partial U}{\partial t} + \frac{\partial F}{\partial x} + \frac{\partial G}{\partial y} + S = 0 \quad (3-1.2)$$

$$\text{where: } U = \begin{bmatrix} \rho \\ \rho u_x \\ \rho u_y \\ E \\ \rho Z \end{bmatrix}, \quad F = \begin{bmatrix} \rho u_x \\ \rho u_x^2 + p \\ \rho u_x u_y \\ (E + p)u_x \\ \rho Z u_x \end{bmatrix}, \quad G = \begin{bmatrix} \rho u_y \\ \rho u_x u_y \\ \rho u_y^2 + p \\ (E + p)u_y \\ \rho Z u_y \end{bmatrix}, \quad S = \begin{bmatrix} 0 \\ 0 \\ 0 \\ 0 \\ r \end{bmatrix}$$

$$E = \frac{p}{\gamma - 1} + Q\rho Z + \frac{1}{2}\rho \vec{u} \cdot \vec{u}$$

$$p = \rho T$$

$$r = -K\rho Z^\nu \exp(E_0/T)$$

At the outflow boundary, the chemical reaction is very close to complete, which means that the mass fraction reactant Z ($Z=1-\lambda$) is very close to zero. Then, the non-reactive dimensionless two-dimensional Euler Equations, Eqs. (3-1.2), become:

$$\frac{\partial U}{\partial t} + \frac{\partial F}{\partial x} + \frac{\partial G}{\partial y} = 0 \quad (3-1.3)$$

$$\text{where: } U = \begin{bmatrix} \rho \\ \rho u_x \\ \rho u_y \\ E \end{bmatrix}, \quad F = \begin{bmatrix} \rho u_x \\ \rho u_x^2 + p \\ \rho u_x u_y \\ (E + p)u_x \end{bmatrix}, \quad G = \begin{bmatrix} \rho u_y \\ \rho u_x u_y \\ \rho u_y^2 + p \\ (E + p)u_y \end{bmatrix}$$

The chemical reaction progress λ ($\lambda=1-Z$) depends upon x for a given set of γ , Q , f , E_0 , and ν . Table 3-1.1 and Fig. 3-1.1 show the relationship between Z and the position in the ZND wave (numbers of $L_{1/2}$) under the following conditions: $\gamma=1.2$, $Q=50$, $f=1.0$, $E_0=10$, $\nu=0.999$.

From table 3-1.1, one can conclude that when the domain length is long enough, the error when making Z equal to 1 is very small. If the error is required to be less than 10^{-5} , the domain length should be over $13.18 L_{1/2}$.

Table 3-1.1: The relationship between Z and position in the ZND wave

Domain Length (No. of $L_{1/2}$)	1-Z	Z
0	0	1
1	0.5	5.00E-01
2	0.742723	2.57E-01
3	0.858366	1.42E-01
4	0.918253	8.17E-02
5	0.951214	4.88E-02
6	0.970112	2.99E-02
7	0.981356	1.86E-02
8	0.988085	1.19E-02
9	0.992621	7.38E-03
10	0.994729	5.27E-03
11	0.996386	3.61E-03
12	0.998043	1.96E-03
13	0.999699	3.01E-04
13.0625	0.999803	1.97E-04
13.15625	0.999958	4.18E-05
13.1875	1	0.00E+00

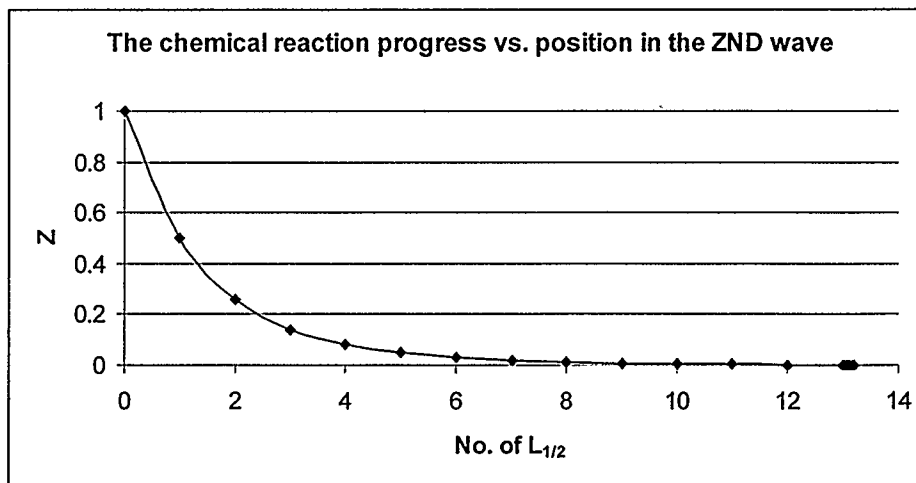


Fig. 3-1.1 The chemical reaction progress vs. position in the ZND wave

3-1-2 Initial Conditions

Well-posed time-dependent initial boundary value problems require an initial condition. However, the extent and nature of the effect of initial conditions are unclear in this irreversible problem. Indeed, the long term solution appears to approach a pattern independent to the initial condition.

A one-dimensional steady ZND profile, to which a multi-dimensional perturbation is added, selected as the initial condition in our simulations. Different perturbations can be used. One approach is to increase the density at eight points around the centre along the y direction, behind leading shock wave, to twice its value, 2ρ . Another one is to add a sinusoidal or cosinusoidal perturbation along the y direction on the velocity u_y , behind the leading shock wave, such as $u_y = U_y \sin \omega y$.

3-1-3 Boundary Conditions

Fig. 3-1.2 illustrates the whole computational domain and boundary conditions.

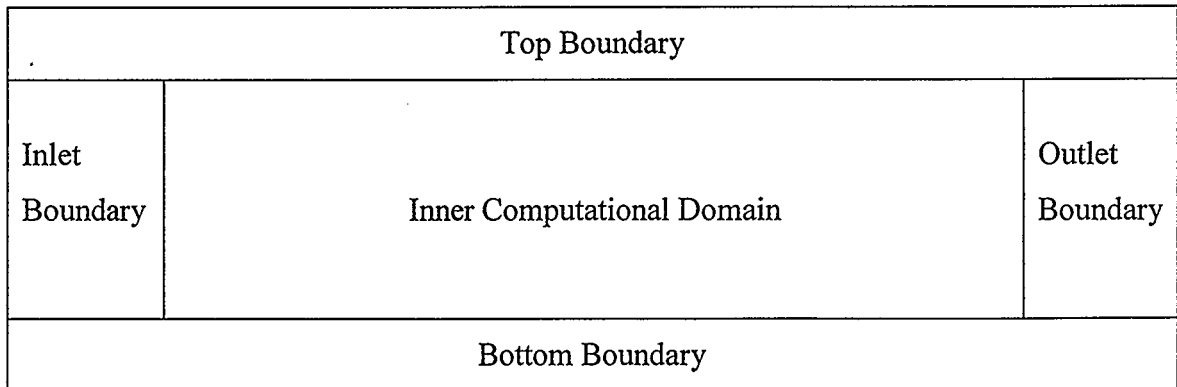


Fig. 3-1.2 Computational domain and boundaries

To keep the domain size to minimum, it is convenient to use a moving frame of reference, attached to the wave. Relative to that frame, the shock is then approximately stationary. For a planar, stationary wave with a given overdrive f and a given heat release Q , the reactant is moving into the shock with velocity:

$$D = \sqrt{f\gamma} \left(\sqrt{1 + \frac{Q(\gamma^2 - 1)}{2\gamma}} + \sqrt{\frac{Q(\gamma^2 - 1)}{2\gamma}} \right)$$

and the other variables are constant with time and y position.

As mentioned above, these inlet boundary conditions correspond to setting a uniform inflow. This requires:

$$\rho_0 = 1, \quad p_0 = 1, \quad Z_0 = 1,$$

$$\rho(0, y, t) = \rho_0 = 1,$$

$$p(0, y, t) = p_0 = 1$$

$$u_x(0, y, t) = u_{x0} = D$$

$$u_y(0, y, t) = u_{y0} = 0$$

$$\rho Z(0, y, t) = \rho_0 Z_0 = 1$$

$$E(0, y, t) = \frac{p_0}{\gamma - 1} + \frac{1}{2} \rho_0 D^2 + \rho_0 Z_0 Q = \frac{1}{\gamma - 1} + \frac{1}{2} D^2 + Q$$

For the outlet boundary condition, a non-reflecting boundary condition is used. This will be discussed in detail in Chapter 4.

For the boundaries at bottom and top, the symmetric boundary condition along y is used, which means that all the variables within the bottom boundary are the same to

symmetric points variables relative to boundary at $y = 1/2$, and all the variables within the top boundary are the same to symmetric points variables relative to boundary at $y = J + 1/2$, in which J are grid points in the y direction.

3-2 Numerical Issues

There are several issues associated with the numerical method, such as monotonicity preservation, conservation, CFL stability criterion, numerical diffusion and numerical errors (round off errors, iteration errors, approximation errors), and so forth.

3-2-1 Numerical Technique

One-dimensional case is used as example. Space is divided into uniform intervals of size Δx and Δy , and time is divided into time intervals Δt $[t^n, t^{n+1}]$. The one-dimensional integral forms of conservation laws are applied to each cell during each time interval and the following is obtained:

$$\int_{x_{i-1/2}}^{x_{i+1/2}} (U^{n+1} - U^n) dx = -\frac{\Delta t}{\Delta x} \left\{ \int_{t^n}^{t^{n+1}} (f_{i+1/2} - f_{i-1/2}) dt \right\} \quad (3-2.1)$$

After introducing flux “F” notation, the numerical conservation can be written as a “flux” form as:

$$U_i^{n+1} = U_i^n - \frac{1}{\Delta x} \{ F_{i+1/2} - F_{i-1/2} \} \quad (3-2.2)$$

Here, F_i are the numerical flux form $\int_{t^n}^{t^{n+1}} f(x_i, t) dt$, which are time-integral averages. All variables at time-step n are known and at time-step n+1 are unknown after n

time steps. There are different schemes to calculate the numerical flux terms. The scheme used in this study are a fifth-order accuracy WENO scheme and fourth-order accuracy scheme. These schemes will be discussed in sections 3-3 and section 3-4. The numerical simulations to resolve the time derivative use the third-order accuracy Runge-Kutta method. These methods will be discussed in section 3-5 and section 3-6.

3-2-2 Monotonicity Preservation

Monotonicity preservation is the property whereby if the initial data before the time step are monotonically increasing, then the numerical solution will be monotonically increasing after that step; and if the initial data are monotonically decreasing, the solution is monotonically decreasing.

A stronger requirement, first suggested by Godunov (1959), is that of monotone schemes, which simply are monotone functions of their arguments. Godunov's theorem explains that linear monotone methods are at best first-order accuracy. In order to achieve high order accuracy, standard higher order finite-differences use linear schemes and this leads to a non-monotone solution near the shock. This results in large oscillations, leading to meaningless results. However, the derivatives do not exist near shocks, so high order accuracy can not be achieved near shock in any event. Instead, non-linear schemes are used, which lead to deterioration of accuracy to first order near shocks but do satisfy a monotonicity requirement. The WENO scheme described below is one such scheme.

3-2-3 Conservation

For an arbitrary volume Ω , bounded by a closed surface S , the integral forms of the conservation laws are:

$$\left\{ \begin{array}{l} \int_{\Omega} [\rho_t + \bar{\nabla} \cdot (\rho \bar{u})] d\Omega = 0 \\ \int_{\Omega} [(\rho \bar{u})_t + \bar{\nabla} \cdot (\rho \bar{u} \otimes \bar{u}) + \bar{\nabla} p] d\Omega = 0 \\ \int_{\Omega} \{E_t + \bar{\nabla} \cdot [(E + p)\bar{u}]\} d\Omega = 0 \end{array} \right. \quad (3-2.3)$$

Because the volumes Ω are arbitrary, the integrands must vanish everywhere. The differential form of the Euler equations can then be obtained after some expansion, assuming all necessary derivatives exist and make sense:

$$\left\{ \begin{array}{l} \frac{\partial \rho}{\partial t} + \frac{\partial(\rho u_x)}{\partial x} + \frac{\partial(\rho u_y)}{\partial y} = 0 \\ \frac{\partial(\rho u_x)}{\partial t} + \frac{\partial(\rho u_x^2)}{\partial x} + \frac{\partial(\rho u_x u_y)}{\partial y} + \frac{\partial p}{\partial x} = 0 \\ \frac{\partial(\rho u_y)}{\partial t} + \frac{\partial(\rho u_x u_y)}{\partial x} + \frac{\partial(\rho u_y^2)}{\partial y} + \frac{\partial p}{\partial y} = 0 \\ \frac{\partial s}{\partial t} + u_x \frac{\partial s}{\partial x} + u_y \frac{\partial s}{\partial y} = 0 \end{array} \right. \quad (3-2.4)$$

After expansion, the energy equation assumes the form of an entropy equation according to which the flow is isentropic. Clearly, this is not valid across shocks. When shocks are present, Eqs. (3-2.3) can not be expanded because when expanding, the required derivatives do not exist.

Comparing Eqs. (3-2.3) with Eqs. (3-2.4), the integral form, Eqs. (3-2.3) determines a unique set of differential equations, but one can show that the reverse is not

true if the flow includes shocks. Still, these two sets of equations have the same solution whenever the flow is smooth. In the current context, the numerical scheme has to be a conservative scheme, which satisfies both the smooth flow and the flow including shocks.

3-2-4 CFL Stability Criterion

For explicit finite difference schemes from von Neumann stability analysis, one can show that the numerical speed of information propagation $u_n = \frac{\Delta x}{\Delta t}$ must be greater than or equal to the physical speed of information propagation $|u_x| + c$, i.e.

$$CFL = (|u_x| + c) \frac{\Delta t}{\Delta x} \leq 1,$$

which leads to a maximum time step:

$$\Delta t_{\max} = \frac{\Delta x}{c + |u_x|}$$

This condition is usually known as the CFL (Courant-Friedrichs-Lewy) stability criterion, recognizing the contribution of these three researchers (1928). Implicit finite numerical schemes are not subject to the CFL stability criterion. Still, accuracy dictates the maximum time step. Typically, in gas dynamics, they are not worth the extra effort and complexity.

3-3 WENO Scheme

The Weighted Essentially Non-Oscillatory (WENO) scheme is used here. This scheme was introduced by Shu & Osher (1988, 1989) and Jiang & Shu (1996, 1999).

WENO schemes belong to the family of ENO (Essentially Non-Oscillatory)

schemes. ENO schemes use the “smoothest” stencil among several candidates to approximate the fluxes at cell boundaries to a high order accuracy while at the same time avoiding spurious oscillations near shocks. Instead of choosing one of the candidate stencils, the WENO method uses a convex combination of all the candidate stencils. Each of the candidate stencils is assigned a weight which determines the contribution of this stencil to the final approximation of the numerical flux. By completely removing the logical statements that appear in the ENO stencil-choosing step, WENO schemes run at least twice as fast as ENO schemes and the fluxes in WENO schemes are smoother than in ENO schemes. In addition, the accuracy of the WENO schemes constructed from the r^{th} -order ENO schemes is of $(2r-1)^{\text{th}}$ -order.

The fifth-order WENO scheme is obtained from $r=3$, as follows, using the one-dimensional Euler equation, Eqs. (3-3.1) as an example:

$$\frac{\partial U}{\partial t} + \frac{\partial F}{\partial x} = 0 \quad (3-3.1)$$

To solve the ordinary differential equation (3-3.2)

$$\frac{\partial U}{\partial t} = L(U) \quad (3-3.2)$$

Dividing space into uniform intervals of size Δx , the spatial operator L of the WENO scheme, which approximates $(-\frac{\partial F}{\partial x})$ at x_i , can be written as:

$$L = -\frac{1}{\Delta x}(\hat{F}_{i+1/2} - \hat{F}_{i-1/2}) \quad (3-3.3)$$

Here \hat{F} is the numerical flux (approximating the physical flux F). To achieve $(2r-1)^{\text{th}}$ -order accuracy approximation, the \hat{F} can be written as:

$$\hat{F}_{i+1/2} = q_{r-1}^{2r-1}(F_{i-r+1}, \dots, F_{i+r-1}) \quad (3-3.4)$$

Assuming that $q_k^r(F_{i+k-r+1}, \dots, F_{i+k})$ ($k=0, 1, \dots, r-1$) are all the candidate stencils and ω_k ($k=0, 1, \dots, r-1$) are weights relative to the candidate stencils, the final approximation of $F_{i+1/2}$ is

$$\hat{F}_{i+1/2} = \sum_{k=0}^{r-1} \omega_k q_k^r(F_{i+k-r+1}, \dots, F_{i+k}) \quad (3-3.5)$$

$$\text{Where: } q_k^r(u_0, \dots, u_{r-1}) = \sum_{l=0}^{r-1} a_{k,l}^r u_l$$

Making sure that the Eqs. (3-3.5) is identical to Eqs. (3-3.4), which is $(2r-1)^{\text{th}}$ – order accuracy, the weight ω_k and coefficient C_k^r are found as follows (Jiang & Shu, 1996):

$$\omega_k = \frac{\alpha_k}{\alpha_0 + \dots + \alpha_{r-1}}, \quad \alpha_k = \frac{C_k^r}{(\varepsilon + IS_k)^p}, \quad \varepsilon = 10^{-10}, \quad p = 2$$

Table 3-3.1: Optimal weights C_k^3 ($r = 3$)

k=0	k=1	k=2
1/10	6/10	3/10

$$IS_0 = \frac{13}{12}(F_{i-2} - 2F_{i-1} + F_i)^2 + \frac{1}{4}(F_{i-2} - 4F_{i-1} + 3F_i)^2$$

$$IS_1 = \frac{13}{12}(F_{i-1} - 2F_i + F_{i+1})^2 + \frac{1}{4}(F_{i-1} - F_{i+1})^2$$

$$IS_2 = \frac{13}{12}(F_i - 2F_{i+1} + F_{i+2})^2 + \frac{1}{4}(3F_i - 4F_{i+1} + F_{i+2})^2$$

Table 3-3.2: Constant coefficients $a_{k,l}^r$ ($r = 3$)

k	l=0	l=1	l=2
0	1/3	-7/6	11/6
1	-1/6	5/6	1/3
2	1/3	5/6	-1/6

3-4 Fourth-Order Spatial Accuracy Method

To match the fifth-order accuracy method in space used in the inner domain, the fourth-order accuracy method in space is needed at boundaries (Poinsot et al. 1992). Using Taylor series, a fourth-order accuracy method is deduced below.

When all variables at time-step n are known and the space derivative $\frac{\partial U_1}{\partial x}$ is constructed, five known variables U_{-3} , U_{-2} , U_{-1} , U_0 , and U_1 at time-step n are used. Expanding them in Taylor series at U_1 , a linear combination of these five points (U_{-3} , U_{-2} , U_{-1} , U_0 , U_1), approximates $\frac{\partial U_1}{\partial x}$, to fourth-order spatial accuracy. Substituting $\frac{\partial U_1}{\partial x}$ into Euler equations and applying non-reflecting BC, one can obtain all variables (U_1) at the outflow boundary. This will be discussed in Chapter 4. (See Fig. 3-4.1)

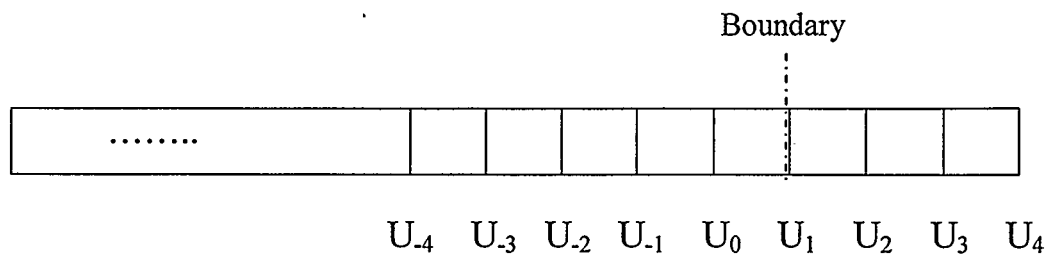


Fig. 3-4.1 Illustration of grid cells

The Taylor series for U at boundary are:

$$U_0 = U_1 - dx * U'_1 + \frac{dx^2}{2} * U''_1 - \frac{dx^3}{6} * U'''_1 + \frac{dx^4}{24} U^{(4)}_1 + 0 * (dx)^4 \quad (1)$$

$$U_{-1} = U_1 - 2dx * U'_1 + \frac{(2dx)^2}{2} * U''_1 - \frac{(2dx)^3}{6} * U'''_1 + \frac{(2dx)^4}{24} U^{(4)}_1 + 0 * (dx)^4 \quad (2)$$

$$U_{-2} = U_1 - 3dx * U'_1 + \frac{(3dx)^2}{2} * U''_1 - \frac{(3dx)^3}{6} * U'''_1 + \frac{(3dx)^4}{24} U^{(4)}_1 + 0 * (dx)^4 \quad (3)$$

$$U_{-3} = U_1 - 4dx * U'_1 + \frac{(4dx)^2}{2} * U''_1 - \frac{(4dx)^3}{6} * U'''_1 + \frac{(4dx)^4}{24} U^{(4)}_1 + 0 * (dx)^4 \quad (4)$$

Combining the four equations by $\alpha_1 * (1) + \alpha_2 * (2) + \alpha_3 * (3) + \alpha_4 * (4)$, setting the coefficients of U''_1 , U'''_1 , and $U^{(4)}_1$ to be zero and the coefficient of U'_1 to be one, then solving α_i ($i = 1, 2, 3, 4$), one can obtain the linear combination that approximates $\frac{\partial U_1}{\partial x}$, which is $U'_1 = -(\alpha_0 U_1 + \alpha_1 U_0 + \alpha_2 U_{-1} + \alpha_3 U_{-2} + \alpha_4 U_{-3})$ and here, $\alpha_0 = \alpha_1 + \alpha_2 + \alpha_3 + \alpha_4$. $\alpha_1 * (1) + \alpha_2 * (2) + \alpha_3 * (3) + \alpha_4 * (4)$ is:

$$\begin{aligned} & \alpha_1 U_0 + \alpha_2 U_{-1} + \alpha_3 U_{-2} + \alpha_4 U_{-3} \\ &= (\alpha_1 + \alpha_2 + \alpha_3 + \alpha_4) * U_1 - (\alpha_1 + 2\alpha_2 + 3\alpha_3 + 4\alpha_4) * dx * U'_1 \\ & \quad + (\alpha_1 + 2^2 \alpha_2 + 3^2 \alpha_3 + 4^2 \alpha_4) * \frac{dx^2}{2} * U''_1 \\ & \quad - (\alpha_1 + 2^3 \alpha_2 + 3^3 \alpha_3 + 4^3 \alpha_4) * \frac{dx^3}{6} * U'''_1 \\ & \quad + (\alpha_1 + 2^4 \alpha_2 + 3^4 \alpha_3 + 4^4 \alpha_4) * \frac{dx^4}{24} * U^{(4)}_1 + 0 * (dx)^4 \end{aligned} \quad (3-4.1)$$

$$\text{setting: } \begin{cases} \alpha_1 + 2\alpha_2 + 3\alpha_3 + 4\alpha_4 = 1 \\ \alpha_1 + 2^2\alpha_2 + 3^2\alpha_3 + 4^2\alpha_4 = 0 \\ \alpha_1 + 2^3\alpha_2 + 3^3\alpha_3 + 4^3\alpha_4 = 0 \\ \alpha_1 + 2^4\alpha_2 + 3^4\alpha_3 + 4^4\alpha_4 = 0 \end{cases} \quad (3-4.2)$$

Solving the Eqs. (3-4.2), one can obtain the linear combination to approximate $\frac{\partial U_1}{\partial x}$ as:

$$\frac{\partial U_1}{\partial x} = \frac{dx}{12} [25 * U_1 - 48 * U_0 + 36 * U_{-1} - 16 * U_{-2} + 3 * U_{-3}] + 0 * (dx)^4$$

Because only one-sided information is available close to the boundaries at time-step $n+1$ for the rest points variables (U_2, U_3, U_4) at outflow boundary, these points can be obtained by a fourth-order scheme, with a linear combination of the five points ahead. The linear combinations that approximate U_2, U_3 , and U_4 are deduced next. For the point U_2 , five known variables U_3, U_2, U_1, U_0 , and U_1 at time-step $n+1$ are used and expanded in Taylor series at U_2 . Setting the coefficients of derivative terms to be zero and the coefficient of U_2 to be one, then solving α_i ($i = 0, 1, 2, 3, 4$), one can obtain the linear combination that approximates U_2 . Replacing the subscript 2 by 3 and 4, the linear combinations that approximate U_3 , and U_4 are obtained.

$$U_1 = U_2 - dx * U_2' + \frac{dx^2}{2} * U_2'' - \frac{dx^3}{6} * U_2''' + \frac{dx^4}{24} U^{(4)}_2 + 0 * (dx)^4 \quad (1)$$

$$U_0 = U_2 - 2dx * U_2' + \frac{(2dx)^2}{2} * U_2'' - \frac{(2dx)^3}{6} * U_2''' + \frac{(2dx)^4}{24} U^{(4)}_2 + 0 * (dx)^4 \quad (2)$$

$$U_{-1} = U_2 - 3dx * U'_2 + \frac{(3dx)^2}{2} * U''_2 - \frac{(3dx)^3}{6} * U'''_2 + \frac{(3dx)^4}{24} U^{(4)}_2 + 0 * (dx)^4 \quad (3)$$

$$U_{-2} = U_2 - 4dx * U'_2 + \frac{(4dx)^2}{2} * U''_2 - \frac{(4dx)^3}{6} * U'''_2 + \frac{(4dx)^4}{24} U^{(4)}_2 + 0 * (dx)^4 \quad (4)$$

$$U_{-3} = U_2 - 5dx * U'_2 + \frac{(5dx)^2}{2} * U''_2 - \frac{(5dx)^3}{6} * U'''_2 + \frac{(5dx)^4}{24} U^{(4)}_2 + 0 * (dx)^4 \quad (5)$$

$$\alpha_0 * (1) + \alpha_1 * (2) + \alpha_2 * (3) + \alpha_3 * (4) + \alpha_4 * (5)$$

$$\begin{aligned} \alpha_0 U_1 + \alpha_1 U_0 + \alpha_2 U_{-1} + \alpha_3 U_{-2} + \alpha_4 U_{-3} &= (\alpha_0 + \alpha_1 + \alpha_2 + \alpha_3 + \alpha_4) * U_2 \\ &- (\alpha_0 + 2\alpha_1 + 3\alpha_2 + 4\alpha_3 + 5\alpha_4) * dx * U'_2 \\ &+ (\alpha_0 + 2^2\alpha_1 + 3^2\alpha_2 + 4^2\alpha_3 + 5^2\alpha_4) * \frac{dx^2}{2} * U''_2 \\ &- (\alpha_0 + 2^3\alpha_1 + 3^3\alpha_2 + 4^3\alpha_3 + 5^3\alpha_4) * \frac{dx^3}{6} * U'''_2 \\ &+ (\alpha_0 + 2^4\alpha_1 + 3^4\alpha_2 + 4^4\alpha_3 + 5^4\alpha_4) * \frac{dx^4}{24} * U^{(4)}_2 + 0 * (dx)^4 \end{aligned} \quad (3-4.1)$$

$$\text{setting: } \begin{cases} \alpha_0 + \alpha_1 + \alpha_2 + \alpha_3 + \alpha_4 = 1 \\ \alpha_0 + 2\alpha_1 + 3\alpha_2 + 4\alpha_3 + 5\alpha_4 = 0 \\ \alpha_0 + 2^2\alpha_1 + 3^2\alpha_2 + 4^2\alpha_3 + 5^2\alpha_4 = 0 \\ \alpha_0 + 2^3\alpha_1 + 3^3\alpha_2 + 4^3\alpha_3 + 5^3\alpha_4 = 0 \\ \alpha_0 + 2^4\alpha_1 + 3^4\alpha_2 + 4^4\alpha_3 + 5^4\alpha_4 = 0 \end{cases}$$

The linear combinations to approximate interior points not at boundary (U_2 , U_3 ,

U_4) are:

$$U_2 = 5*U_1 - 10*U_0 + 10*U_{-1} - 5*U_{-2} + U_{-3} + 0*(dx)^4$$

$$U_3 = 5*U_2 - 10*U_1 + 10*U_0 - 5*U_{-1} + U_{-2} + 0*(dx)^4$$

$$U_4 = 5*U_3 - 10*U_2 + 10*U_1 - 5*U_0 + U_{-1} + 0*(dx)^4$$

3-5 Third-Order Accuracy Runge-Kutta Method

Runge-Kutta methods are a family of single-point methods for solving non-linear first-order ordinary differential equation (ODE) problems. The third-order Total Variation Diminishing (TVD) Runge-Kutta method used in this study is as follows (Jiang & Shu 1996):

$$\frac{dU_i}{dt} = L(U)_i$$

$$U_i^{(1)} = U_i^n + \Delta t * L(U^n)_i$$

$$U_i^{(2)} = \frac{3}{4}U_i^n + \frac{1}{4}U_i^{(1)} + \frac{1}{4} * \Delta t * L(U^{(1)})_i$$

$$U_i^{n+1} = \frac{1}{3}U_i^n + \frac{2}{3}U_i^{(2)} + \frac{2}{3}\Delta t * L(U^{(2)})_i$$

3-6 Second-Order Accuracy Method

To match the third-order accuracy method in time used in the inner computational domain, the four-step second-order method in time used at the boundaries, Thompson (1979), is selected as following:

$$\frac{dU_i}{dt} = L(U)_i$$

$$U_i^{(1)} = U_i^n + \frac{1}{4} * \Delta t * L(U^n)_i$$

$$U_i^{(2)} = U_i^n + \frac{1}{3} * \Delta t * L(U^{(1)})_i$$

$$U_i^{(3)} = U_i^n + \frac{1}{2} * \Delta t * L(U^{(2)})_i$$

$$U_i^{n+1} = U_i^n + \Delta t * L(U^{(3)})_i$$

3-7 Implementation

The schemes discussed above are finite-volume numerical approximations based directly on the conservation form. The fluxes in x direction and y direction can be obtained by using the schemes described in section 3-3 and section 3-4. Submit them into Eqs. (3-3.2). By using schemes described in section 3-5 and section 3-6, the next time-step variables U^{n+1} can be obtained. In this way, arbitrary time-step and spatial index variables $U_{(i,j)}^n$ will be obtained which are the approximations of analytical solutions $U_{(x,y,t)}$ respectively.

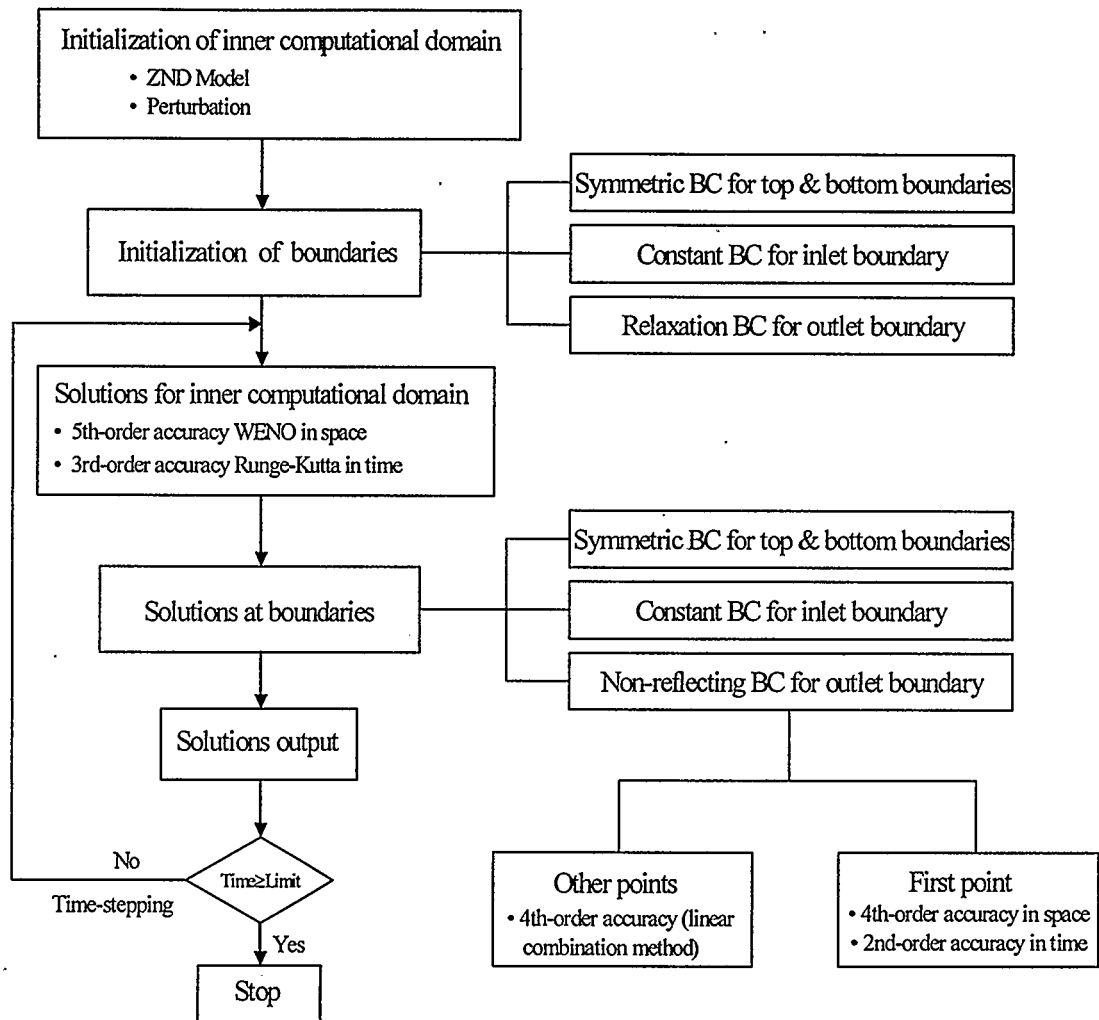


Fig. 3-7.1 Flowchart of the detonation simulation

THE CHARACTERISTICS METHOD

4-1 Introduction

Because computational domains are unavoidably finite, long or infinite physical domains require truncation, resulting in artificial boundaries. To minimize reflection of outgoing disturbances, non-reflecting numerical boundary conditions are needed at these artificial boundaries.

There are several ways to construct non-reflecting boundary conditions (BCs), belonging to four categories: the characteristics-based method; far field asymptotic solutions; the buffer zone technique; the perfectly matched layer technique (PML).

Main contributors to the characteristics method are Hedstrom (1979), Thompson (1979, 1990), Higdon (1987), Giles (1990), and Poinsot & Lele (1992). This is a straightforward method. All the conservation equations are rewritten into a set of wave equations and all the incoming waves are set to be constant, while all the outgoing waves

travel smoothly out at the non-reflecting BC. This is the method that has been selected here and a more detailed discussion is included below.

Far Field Asymptotic Solutions have been studied by a number of researchers, including Enquist & Majda (1977), Bayliss & Turkel (1980, 1982), Hagstrom & Hariharan (1988), and Tam & Webb (1993). This method is based upon the concept of radiation boundary conditions. If the problem has wave-like solutions near infinity, these boundary conditions must simulate the radiation of energy out of the computational domain and towards infinity. If the time-dependent equations are only an intermediate step toward computing a steady state, a flow of energy into the computational domain can delay convergence. In the far field, the non-linear equations are often reduced to some simple forms, such as wave equations. This method relies upon using an asymptotic solution. It is very accurate but the drawback is that asymptotic solutions are required, which may not be easy to obtain, and the computational cost could be high.

Buffer Zone Techniques have been developed in the last twenty years. In these techniques, a buffer zone is created to damp the reflection. Different techniques are used in the buffer zone. For instance, Israeli & Orszag (1981), Colonius, and Lele & Moin (1993) use low-pass filters or grid stretching to damp the numerical solution. In contrast to this technique, Streett & Macaraeg (1989) and Ta'asan & Nark (1995) make the mean flow accelerate to supersonic at the end of the buffer domain thus making that boundary naturally non-reflecting. The accuracy of these methods depends upon how gradually the parameters vary inside the buffer zone. These methods are computationally costly as well.

The Perfectly Matched Layer (PML) is a new method of constructing a non-reflecting boundary condition. It is based on the Perfectly Matched Layer technique. Similar to the buffer zone method, an extra layer is created in which the outgoing

waves are damped or “absorbed.” This method was first introduced by Berenger (1994) for absorbing electromagnetic wave solutions of the Maxwell equations. Hu (1996, 2002) extended this method for spatially varying absorption coefficients. This method is very effective because it requires a small number of grid points to achieve satisfactory results. However, it only works for linear equations.

In summary, Far Field Asymptotic Solutions and the Buffer Zone Technique are very accurate methods, but their computational costs are considerably high. In addition, the asymptotic forms are not always available. The PML technique costs less computationally, but it is suitable for linear equations only. Here, the characteristics method is selected because it provides a reasonable trade off between performance and cost and it meets our accuracy requirement. The method is described in detail in the following sections.

4-2. Characteristic Form of the One-dimensional Euler Equations

For time-dependent problems, Hedstrom (1979) was the first to develop the characteristics method for the one dimensional rectangular non-linear case. Thompson (1979, 1990) extended this concept to the multi-dimensional case in non-rectangular coordinate systems. In this research, based on K. W. Thompson’s study, higher order accuracy schemes are implemented and a more complete evaluation of the results is carried out.

As mentioned in section 4-1, the characteristics method is based upon rewriting the conservation laws as a set of wave equations and setting every incoming Riemann variable to a constant value, which means no incoming waves, hence no reflection.

First, consider the one-dimensional flow in Cartesian coordinates. The non-linear Euler equations can then be written in conservative form as:

$$\frac{\partial \tilde{U}}{\partial t} + \frac{\partial F}{\partial x} + C' = 0 \quad (4-2.1)$$

or in the primitive variable form as:

$$\frac{\partial U}{\partial t} + A \frac{\partial U}{\partial x} + C = 0 \quad (4-2.2)$$

Here C' and C are inhomogeneous source terms, not containing derivatives. In our case, C is zero. A is a $n \times n$ matrix and U are the primitive variables:

$$U = \begin{bmatrix} \rho \\ u \\ s \end{bmatrix} \quad A = \begin{bmatrix} u & \rho & 0 \\ \frac{c^2}{\rho} & u & \frac{p}{\rho s} \\ 0 & 0 & u \end{bmatrix}$$

A is diagonalizable and can be put in the diagonal form J by the similarity transformations: $J = SAS^{-1}$. Here, S and S^{-1} are the left and right eigenvectors of A . Then J is:

$$J = \begin{bmatrix} u-c & 0 & 0 \\ 0 & u & 0 \\ 0 & 0 & u+c \end{bmatrix}$$

Next, the non-linear Euler equations are rewritten into characteristic form, yielding Eqs. (4-2.3):

$$S \frac{\partial U}{\partial t} + JS \frac{\partial U}{\partial x} = 0 \quad (4-2.3)$$

or in the component characteristic form, Eqs. (4-2.4):

$$\frac{\partial V_i}{\partial t} + \lambda_i \frac{\partial V_i}{\partial x} = 0 \quad (4-2.4)$$

Let I_i be the set of left eigenvectors of A, then $dV_i = I_i dU$.

This is a set of wave equations. Waves can be categorized into incoming waves and outgoing waves. At the inlet boundary, when $\lambda_i > 0$, the waves are incoming waves; when $\lambda_i < 0$, the waves are outgoing waves. At the outlet boundary, when $\lambda_i > 0$, the waves are outgoing waves; when $\lambda_i < 0$, the waves are incoming waves.

Eliminating s in favor of p , ρ and u , Eqs.(4-2.4) can be written as Eqs. (4-2.5)

$$\begin{cases} \left(\frac{\partial p}{\partial t} - \rho c \frac{\partial u}{\partial t} \right) + (u - c) \left(\frac{\partial p}{\partial x} - \rho c \frac{\partial u}{\partial x} \right) = 0 \\ \left(\frac{\partial p}{\partial t} + \rho c \frac{\partial u}{\partial t} \right) + (u + c) \left(\frac{\partial p}{\partial x} + \rho c \frac{\partial u}{\partial x} \right) = 0 \\ \left(\frac{\partial p}{\partial t} - c^2 \frac{\partial \rho}{\partial t} \right) + u \left(\frac{\partial p}{\partial x} - c^2 \frac{\partial \rho}{\partial x} \right) = 0 \end{cases} \quad (4-2.5)$$

Based on Hedstrom's (1979) concept, a non-reflecting boundary condition is defined as one in which the amplitude of the incoming waves is constant in time at the non-reflecting boundary. Assume the computational domain is the range of values of x between a and b ($a < x < b$). Then, the non-reflecting boundary condition can be expressed mathematically in the following form:

For inlet boundary ($x = a$), when $\lambda_i > 0$, $\frac{\partial V_i}{\partial t} \Big|_{x=a} = 0$

For outlet boundary ($x = b$), when $\lambda_i < 0$, $\frac{\partial V_i}{\partial t} \Big|_{x=b} = 0$

In a general form, the characteristic and non-reflecting boundary condition can be combined into:

$$I_i \frac{\partial U_i}{\partial t} + L_i = 0 \quad (4-2.6)$$

$$\text{where } L_i = \begin{cases} 0 & \text{for incoming waves} \\ \lambda_i I_i \frac{\partial U_i}{\partial x} & \text{for outgoing waves} \end{cases} \quad (4-2.7)$$

Given the L_i values, the time derivatives of the primitive variables are:

$$\begin{cases} \frac{\partial p}{\partial t} = -\frac{1}{2}(L_3 + L_1) \\ \frac{\partial u}{\partial t} = \frac{1}{2\rho c}(L_3 - L_1) \\ \frac{\partial \rho}{\partial t} = \frac{1}{c^2}\left(\frac{\partial p}{\partial t} + L_2\right) \end{cases} \quad (4-2.8)$$

The relationship between the time derivatives of the primitive variables and the time derivatives of the conservative variables is shown in Eqs. (4-2.9):

$$\left\{ \begin{array}{l} \frac{\partial \rho}{\partial t} = \frac{\partial \rho}{\partial t} \\ \frac{\partial(\rho u)}{\partial t} = u \frac{\partial \rho}{\partial t} + \rho \frac{\partial u}{\partial t} \\ \frac{\partial e}{\partial t} = \frac{1}{2} u^2 \frac{\partial \rho}{\partial t} + \rho u \frac{\partial u}{\partial t} + \frac{1}{\gamma - 1} \frac{\partial p}{\partial t} \end{array} \right. \quad (4-2.9)$$

Integrating Eqs. (4-2.9) with the second-order accuracy method discussed in section 3-6, all the conservative variables at the outflow boundary can be obtained.

Theoretically, setting all incoming waves to be constant makes the boundary fully non-reflecting. Numerically, however, only an approximation is obtained. The actual reflection rate depends on numerical factors, such as schemes, the length of computational domain, and so forth.

4-3. Riemann Invariants

The characteristic form of the non-linear Euler equations, Eqs. (4-2.5), can also be rewritten as follows:

$$\left\{ \begin{array}{l} \frac{\partial V_-}{\partial t} + (u - c) \frac{\partial V_-}{\partial x} = 0 \\ \frac{\partial V_0}{\partial t} + u \frac{\partial V_0}{\partial x} = 0 \\ \frac{\partial V_+}{\partial t} + (u + c) \frac{\partial V_+}{\partial x} = 0 \end{array} \right. \quad (4-3.1)$$

$$\text{where } \begin{cases} dV_- = du - \frac{dp}{\rho c} \\ dV_0 = d\rho - \frac{dp}{c^2} \\ dV_+ = du + \frac{dp}{\rho c} \end{cases}$$

Then, rewriting Eqs. (4-3.1),

$$\begin{cases} dV_- = du - \frac{dp}{\rho c} = 0 & \text{on the characteristic } dx = (u - c)dt \\ dV_0 = d\rho - \frac{dp}{c^2} = 0 & \text{on the characteristic } dx = udt \\ dV_+ = du + \frac{dp}{\rho c} = 0 & \text{on the characteristic } dx = (u + c)dt \end{cases} \quad (4-3.2)$$

The special case in which entropy is spatially uniform is of some interest. Then s is constant everywhere and not just along the characteristic curves $dx=u dt$. For a perfect gas, we have:

$$\frac{p}{\rho^\gamma} = \text{const.} \quad \text{and} \quad \frac{c}{\rho^{\frac{\gamma-1}{2}}} = \text{const.}$$

A short calculation can prove that

$$\int \frac{dp}{\rho c} = \frac{2c}{\gamma-1} + \text{const.} \quad (4-3.3)$$

Then, integrating and combining with Eq. (4-3.3), Eqs. (4-3.2) become:

$$\left\{ \begin{array}{l} s = \text{const.} \\ V_- = u - \frac{2c}{\gamma - 1} = \text{const.} \quad \text{on} \quad dx = (u - c)dt \\ V_+ = u + \frac{2c}{\gamma - 1} = \text{const.} \quad \text{on} \quad dx = (u + c)dt \end{array} \right. \quad (4-3.4)$$

The characteristic variables V_{\pm} are also known as the Riemann invariants. For isentropic flow, Eqs. (4-3.1) show that the Riemann invariants are constant along their respective characteristic lines.

4-4. Characteristic Form of the Two-dimensional Euler Equations

The standard conservation equations for two-dimensional flow can be written in the form of:

$$\frac{\partial \tilde{U}}{\partial t} + \frac{\partial F}{\partial x} + \frac{\partial G}{\partial y} + C_x' + C_y' = 0 \quad (4-4.1)$$

Eqs. (4-4.1) can be rewritten in non-conservative form as:

$$\frac{\partial U}{\partial t} + A \frac{\partial U}{\partial x} + B \frac{\partial U}{\partial y} + C_x + C_y = 0 \quad (4-4.2)$$

According to the assumptions that the flow is inviscid and non-heat-conducting and that the chemical reaction is complete at the outflow boundary, Eqs. (4-4.2) can be simplified to

$$\frac{\partial U}{\partial t} + A \frac{\partial U}{\partial x} + B \frac{\partial U}{\partial y} = 0 \quad (4-4.3)$$

Assuming the λ_i are eigenvalues of A , μ_i are eigenvalues of B , S_i and S_i^{-1} are left and right eigenvectors of A for λ_i , T_i and T_i^{-1} are left and right eigenvectors of B for μ_i , the matrices A and B can be put in the diagonal forms J and K by the similarity transformations:

$$J = SAS^{-1}, \quad K = TBT^{-1}$$

Then, Eqs. (4-4.3) can be written as :

$$\frac{\partial U}{\partial t} + S^{-1}JS \frac{\partial U}{\partial x} + T^{-1}KT \frac{\partial U}{\partial y} = 0 \quad (4-4.4)$$

Let us consider boundaries where x is constant ($x=a$, $x=b$) with the index $i = 0$, $i = I+1$, in which I is the grid points in x direction. The y derivative can be evaluated numerically as an interior term. The x derivative is in the normal direction and must be put in characteristic form so that the appropriate boundary conditions can be imposed at the x boundaries:

$$\frac{\partial \tilde{U}}{\partial t} + \frac{\partial G}{\partial y} + S^{-1}JS \frac{\partial U}{\partial x} = 0 \quad (4-4.5)$$

Abbreviating the quantity $JS \frac{\partial U}{\partial x}$ as $-\partial U / \partial t_x$, we must evaluate $\partial U / \partial t_x$ in Eqs. (4-4.6)

$$S \frac{\partial U}{\partial t_x} + JS \frac{\partial U}{\partial x} = 0 \quad (4-4.6)$$

To provide boundary conditions for Eqs. (4-4.6) at x boundaries, let us define the quantity L_i :

$$L_i = \begin{cases} \lambda_i S_i \frac{\partial U}{\partial x} & \text{for outgoing waves} \\ 0 & \text{for incoming waves} \end{cases}$$

Given $\partial U / \partial t_x$, $\partial \tilde{U} / \partial t$ can be computed from Eqs. (4-4.7)

$$\frac{\partial \tilde{U}}{\partial t} + \frac{\partial G}{\partial y} - S \frac{\partial U}{\partial t_x} = 0 \quad (4-4.7)$$

Here, the y derivatives are evaluated in conservative forms and the x direction terms are put in characteristic form.

Two-dimensional Euler equations, Eqs. (4-4.1) can be written in the components form:

$$\left\{ \begin{aligned} \frac{\partial \rho}{\partial t} + \frac{\partial(\rho u_x)}{\partial x} + \frac{\partial(\rho u_y)}{\partial y} &= 0 \\ \frac{\partial(\rho u_x)}{\partial t} + \frac{\partial(\rho u_x^2)}{\partial x} + \frac{\partial(\rho u_x u_y)}{\partial y} + \frac{\partial p}{\partial x} &= 0 \\ \frac{\partial(\rho u_y)}{\partial t} + \frac{\partial(\rho u_x u_y)}{\partial x} + \frac{\partial(\rho u_y^2)}{\partial y} + \frac{\partial p}{\partial y} &= 0 \\ \frac{\partial s}{\partial t} + u_x \frac{\partial s}{\partial x} + u_y \frac{\partial s}{\partial y} &= 0 \end{aligned} \right. \quad (4-4.8)$$

$$p = p^\gamma (\gamma - 1) e^{\frac{s - s_0}{c_v}} \quad c = \left(\frac{p}{\rho} \right)^{1/2}$$

$$\therefore U = \begin{bmatrix} \rho \\ u_x \\ u_y \\ s \end{bmatrix} \quad A = \begin{bmatrix} u_x & \rho & 0 & 0 \\ \frac{c^2}{\rho} & u_x & 0 & \frac{p}{\rho s} \\ 0 & 0 & u_x & 0 \\ 0 & 0 & 0 & u_x \end{bmatrix} \quad B = \begin{bmatrix} u_y & 0 & \rho & 0 \\ 0 & u_y & 0 & 0 \\ \frac{c^2}{\rho} & 0 & u_y & \frac{p}{\rho s} \\ 0 & 0 & 0 & u_y \end{bmatrix}$$

$$\begin{cases} \lambda_1 = u_x - c \\ \lambda_2 = \lambda_3 = u_x \\ \lambda_4 = u_x + c \end{cases} \quad \begin{cases} \mu_1 = u_y - c \\ \mu_2 = \mu_3 = u_y \\ \mu_4 = u_y + c \end{cases}$$

The left eigenvectors of A are:

$$S_1 = (-c, \rho, 0, -\frac{p}{sc}) \quad S_2 = (0, 0, 1, 0)$$

$$S_3 = (0, 0, 0, 1) \quad S_4 = (c, \rho, 0, \frac{p}{sc})$$

The characteristic equations in x direction are Eqs. (4-4.9).

$$\left\{ \begin{array}{l} \left(\frac{\partial p}{\partial t_x} - \rho c \frac{\partial u_x}{\partial t_x} \right) + \lambda_1 \left(\frac{\partial p}{\partial x} - \rho c \frac{\partial u_x}{\partial x} \right) = 0 \\ \frac{\partial u_y}{\partial t_x} + \lambda_2 \frac{\partial u_y}{\partial x} = 0 \\ \left(\frac{\partial p}{\partial t_x} - c^2 \frac{\partial \rho}{\partial t_x} \right) + \lambda_3 \left(\frac{\partial p}{\partial x} - c^2 \frac{\partial \rho}{\partial x} \right) = 0 \\ \left(\frac{\partial p}{\partial t_x} + \rho c \frac{\partial u_x}{\partial t_x} \right) + \lambda_4 \left(\frac{\partial p}{\partial x} + \rho c \frac{\partial u_x}{\partial x} \right) = 0 \end{array} \right. \quad (4-4.9)$$

By using non-reflecting BC

$$\text{Let } L_i = \begin{cases} \lambda_i I_i \frac{\partial U}{\partial x} & \text{for outgoing waves} \\ 0 & \text{for incoming waves} \end{cases}$$

L_1 , L_2 , L_3 , and L_4 can be obtained. Substituting them into Eqs. (4-4.9):

$$\left\{ \begin{array}{l} \left(\frac{\partial p}{\partial t_x} - \rho c \frac{\partial u_x}{\partial t_x} \right) + L_1 = 0 \\ \frac{\partial u_y}{\partial t_x} + L_2 = 0 \\ \left(\frac{\partial p}{\partial t_x} - c^2 \frac{\partial \rho}{\partial t_x} \right) + L_3 = 0 \\ \left(\frac{\partial p}{\partial t_x} + \rho c \frac{\partial u_x}{\partial t_x} \right) + L_4 = 0 \end{array} \right. \quad (4-4.10)$$

Rearranging Eqs. (4-4.10), the time derivatives of pressure, density and velocity can be obtained as in function of the L_i . Eqs. (4-4.11):

$$\left\{ \begin{array}{l} \frac{\partial p}{\partial t_x} = -\frac{1}{2}(L_4 + L_1) \\ \frac{\partial u_x}{\partial t_x} = \frac{1}{2\rho c}(L_4 - L_1) \\ \frac{\partial u_y}{\partial t_x} = -L_2 \\ \frac{\partial \rho}{\partial t_x} = \frac{1}{c^2}\left(\frac{\partial p}{\partial t} + L_3\right) \end{array} \right. \quad (4-4.11)$$

The time derivatives of the conservative variables can be obtained, Eqs. (4-4.12):

$$\left\{ \begin{array}{l} \frac{\partial \rho}{\partial t_x} = \frac{\partial \rho}{\partial t_x} \\ \frac{\partial(\rho u_x)}{\partial t_x} = u_x \frac{\partial \rho}{\partial t_x} + \rho \frac{\partial u_x}{\partial t_x} \\ \frac{\partial(\rho u_y)}{\partial t_x} = u_y \frac{\partial \rho}{\partial t_x} + \rho \frac{\partial u_y}{\partial t_x} \\ \frac{\partial e}{\partial t_x} = \frac{1}{2}(u_x^2 + u_y^2) \frac{\partial \rho}{\partial t_x} + \rho(u_x \frac{\partial u_x}{\partial t_x} + u_y \frac{\partial u_y}{\partial t_x}) + \frac{1}{\gamma - 1} \frac{\partial p}{\partial t_x} \end{array} \right. \quad (4-4.12)$$

Substituting Eqs. (4-4.12) into Eqs. (4-4.7), rewriting them into the components form, Eqs. (4-4.13) are obtained.

$$\left\{ \begin{array}{l} \frac{\partial \rho}{\partial t} - \frac{\partial \rho}{\partial t_x} + \frac{\partial(\rho u_y)}{\partial y} = 0 \\ \frac{\partial(\rho u_x)}{\partial t} - \frac{\partial(\rho u_x)}{\partial t_x} + \frac{\partial(\rho u_y^2)}{\partial y} = 0 \\ \frac{\partial(\rho u_y)}{\partial t} - \frac{\partial(\rho u_y)}{\partial t_x} + \frac{\partial(\rho u_y u_x)}{\partial y} + \frac{\partial p}{\partial y} = 0 \\ \frac{\partial e}{\partial t} - \frac{\partial e}{\partial t_x} + \frac{\partial}{\partial y}[(e + p)u_y] = 0 \end{array} \right. \quad (4-4.13)$$

Using the numerical techniques and schemes discussed in Chapter 3 to integrate conservative variables, one can obtain the numerical conservative variables $\tilde{U}_{(i,j)}^n$, which are the approximation of analytical conservative variables $\tilde{U}_{(x,y,t)}$ and satisfies non-reflecting boundary condition at out flow in the x direction.

VALIDATION

The characteristics-based non-reflecting boundary condition proposed by Hedstrom (1979) has been implemented in our code. Since exact solutions can be obtained for many one-dimensional unsteady flows, we use various one-dimensional test cases with no chemical reaction to demonstrate the effectiveness of the method. The various problems used for validation include the pressure impulse test and the shock tube test. Results and discussion are presented in this section.

In all the tests, within the inner computational domain, the Euler equations are solved by a fifth-order WENO scheme (Jiang & Shu 1996) for spatial derivatives and a third-order Runge-Kutta scheme (Hoffman 2001) in time. At the boundaries, a one-sided fourth-order scheme for spatial derivatives and a second-order scheme (Thompson 1979) for time derivatives have been implemented. In addition, in all cases, a ratio of specific heats of 1.2, a rate law ν of 0.999, and a Courant number of 0.4 have been used. (See Chapter 3).

5-1 Pressure Impulse Test

A qualitative pressure impulse test is computed with the following initial conditions:

1. A pressure peak with height of 20% above the surrounding pressure is placed at the center of the domain;
2. The flow is convected from the left hand to the right hand side with a dimensionless velocity of 0.5 (see Fig. 5-1.1);
3. To keep the temperatures constant along x , density has the same peak as pressure at the same position.

Fig. 5-1.2, Fig. 5-1.3, and Fig. 5-1.4 depict the plots of pressure and total energy at three instants, before, when and after the disturbance crosses right boundary respectively. The results in the figures show that no reflection appears at the right boundary when the wave crosses it.

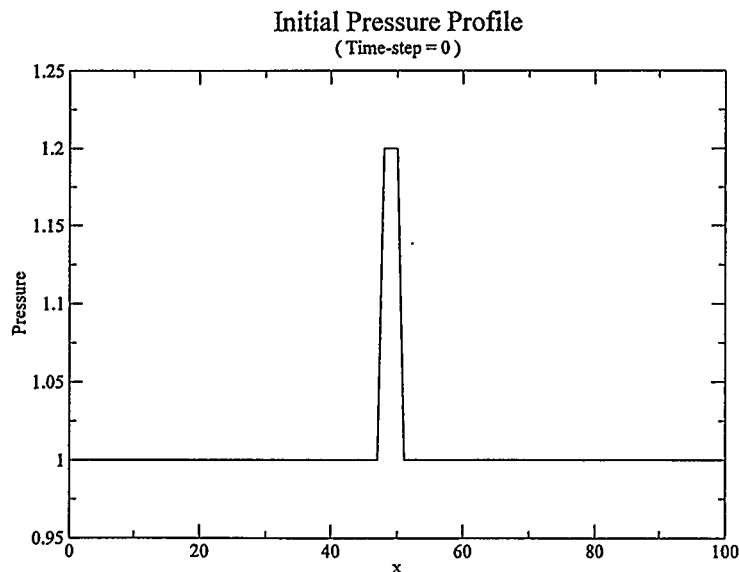


Fig. 5-1.1 Initial pressure profile

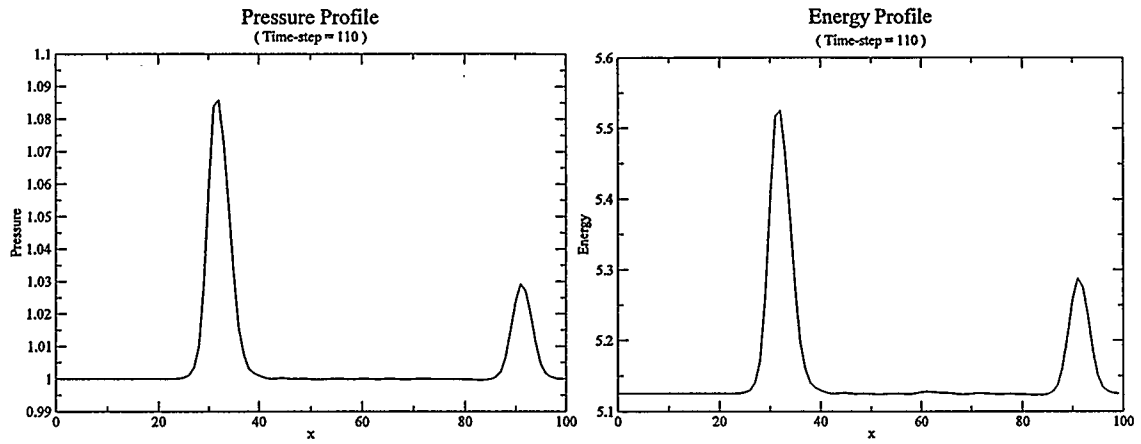


Fig. 5-1.2 Pressure and total energy profiles before the disturbance crosses the outlet

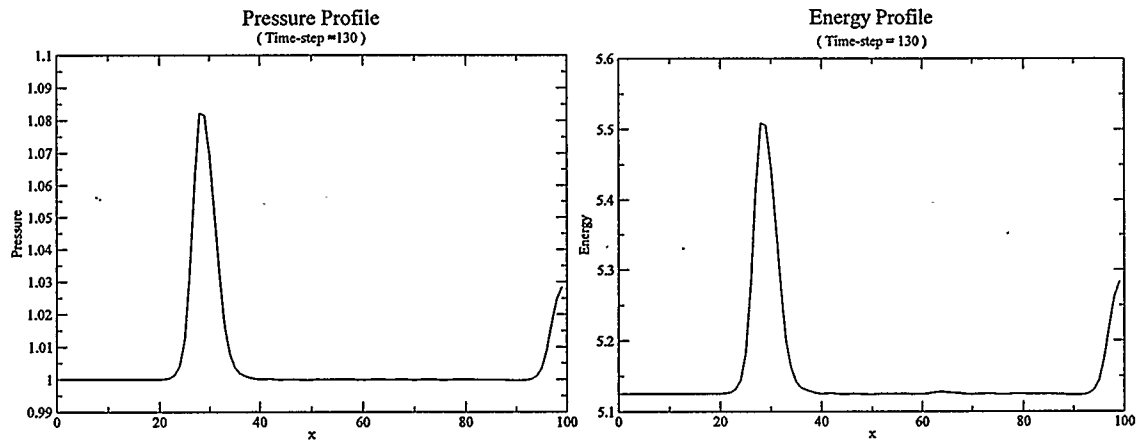


Fig. 5-1.3 Pressure and total energy profiles when the disturbance crosses the outlet

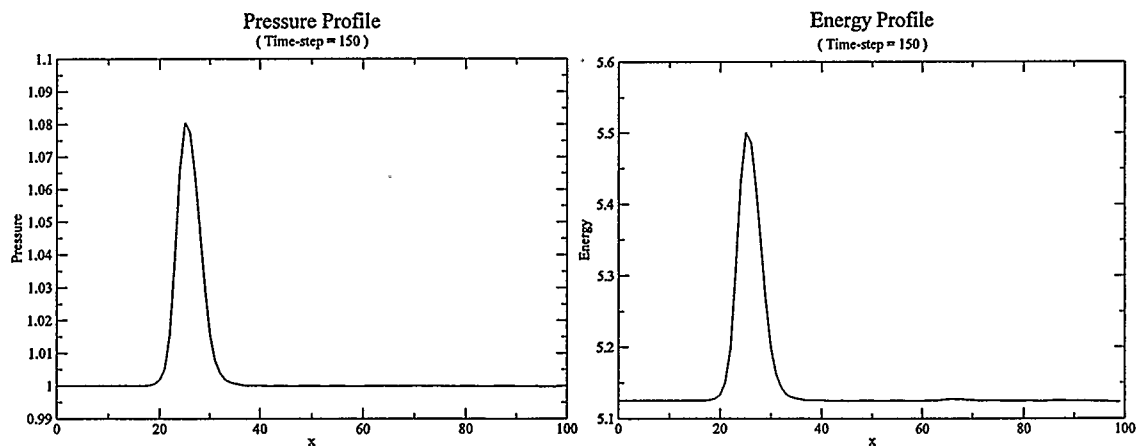


Fig. 5-1.4 Pressure and total energy profiles after the disturbance crosses the outlet

5-2 Shock Tube Test

Shock tube problems consider the evolution of initial one-dimensional discontinuities. Physically, the shock tube is a device in which normal shock waves and expansion waves are generated by the rupture of a diaphragm separating a high-pressure gas from one at low pressure. The solution can always be constructed by self-similarity for times before waves reach extremities; this is the Riemann problem. Here, it is assumed that the diaphragm is initially placed at the center of the computational domain. The initial condition at left side is a high-pressure with $u = 0$, while the right side is at low pressure also with $u = 0$. The diaphragm rupture occurs at $t=0$.

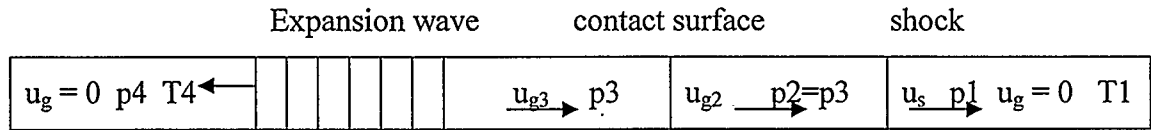


Fig. 5-2.1 Illustration of the shock tube solution

Here, T_1 and T_4 are taken to be equal. Also, $p_2 = p_3$. The solution is determined by the pre- and post-shock values of ρ , p and u , and the shock velocity u_s . It must satisfy the three shock jump conditions as follows:

$$\frac{p_1}{p_4} = \frac{1}{R} \left[1 - \frac{\gamma - 1}{2\gamma} \frac{(R - 1)}{\sqrt{1 + \frac{\gamma + 1}{2\gamma} (R - 1)}} \right]^{2\gamma / (\gamma - 1)} \quad (5-2.1)$$

Here R is the pressure ratio p_2 / p_1 (before and after shock pressure).

There is one free parameter, the chosen pressure R . The relationship between the Mach number of the post-shock flow (u_{g2}/c_1) and R is:

$$M^2 = \frac{2}{\gamma R} \frac{(R-1)^2}{\gamma + 1 + (\gamma-1)/R} \quad (5-2.2)$$

The initial condition is shown in Fig. 5-2.2. After the diaphragm ruptures, a shock wave appears and moves right, while an expansion wave moves left as shown in Fig. 5-2.1. Fig. 5-2.3 illustrates the distribution of density, pressure, temperature, velocity, Riemann variable (m), and Riemann variable (n) after the shock crosses the right boundary and Fig. 5-2.4 shows the expansion wave is crossing the left boundary.

From Fig. 5-2.3, one can see that when the non-reflecting boundary condition is used at both boundaries. There is no visible reflection when the shock wave crosses the right boundary or when the expansion wave crosses the left boundary. A quantitative reflection analyses, in which the value of the small remaining reflection is examined, are presented in section 5-3 and section 5-4.

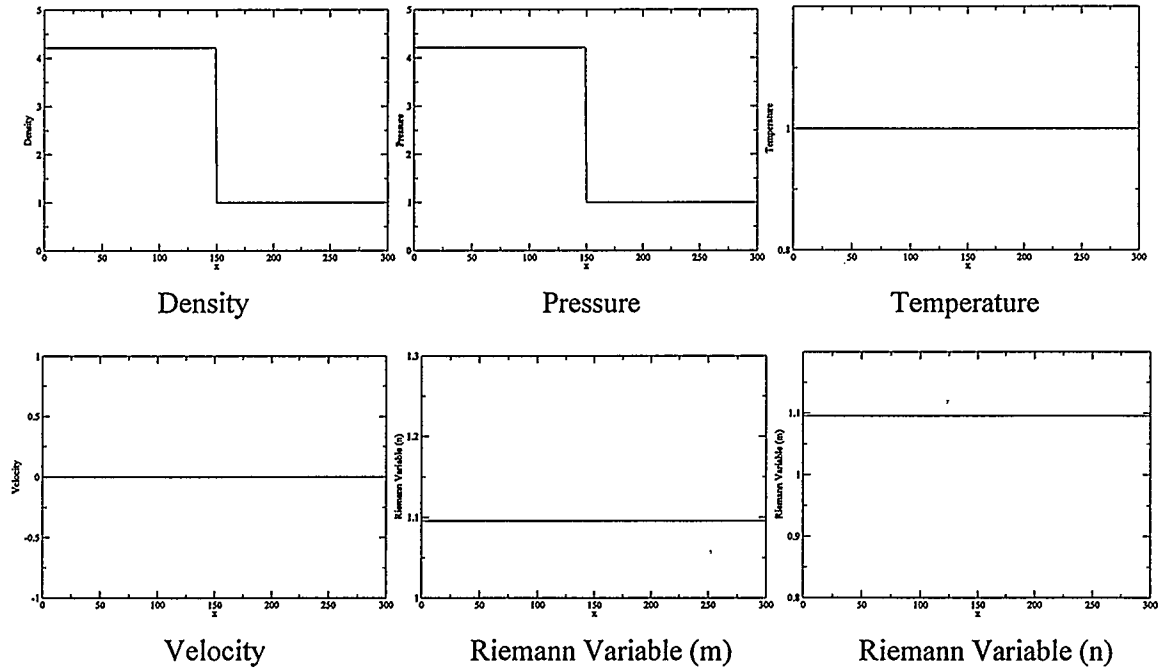


Fig. 5-2.2 Shock tube at time-step 0.

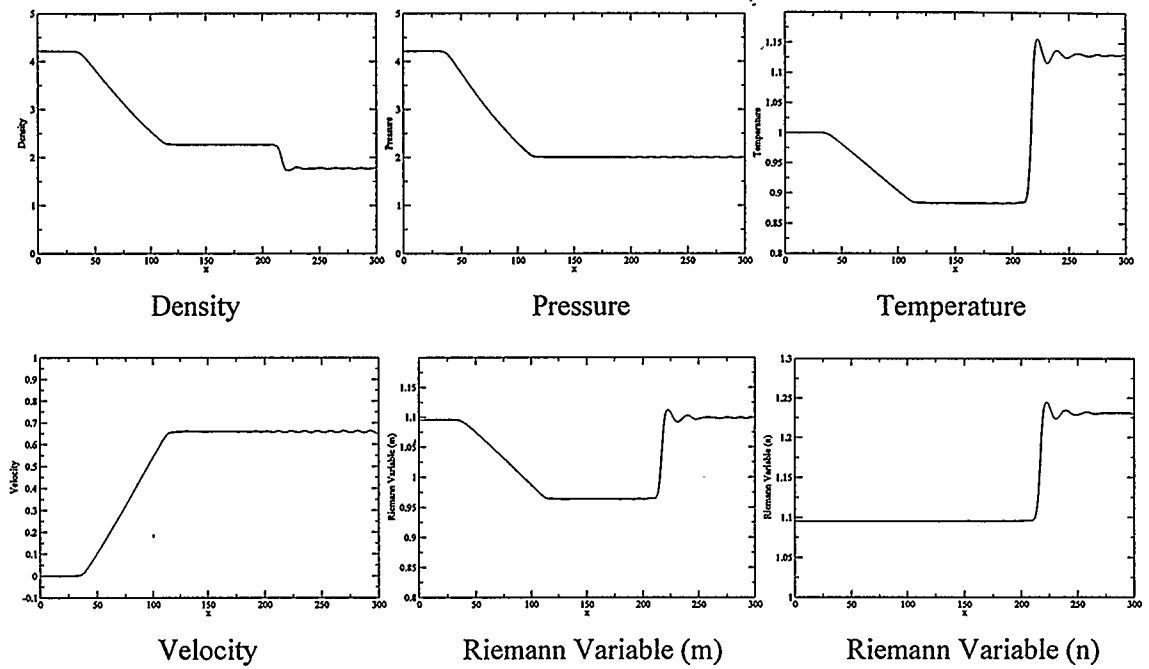


Fig. 5-2.3 Shock tube at time-step 1140

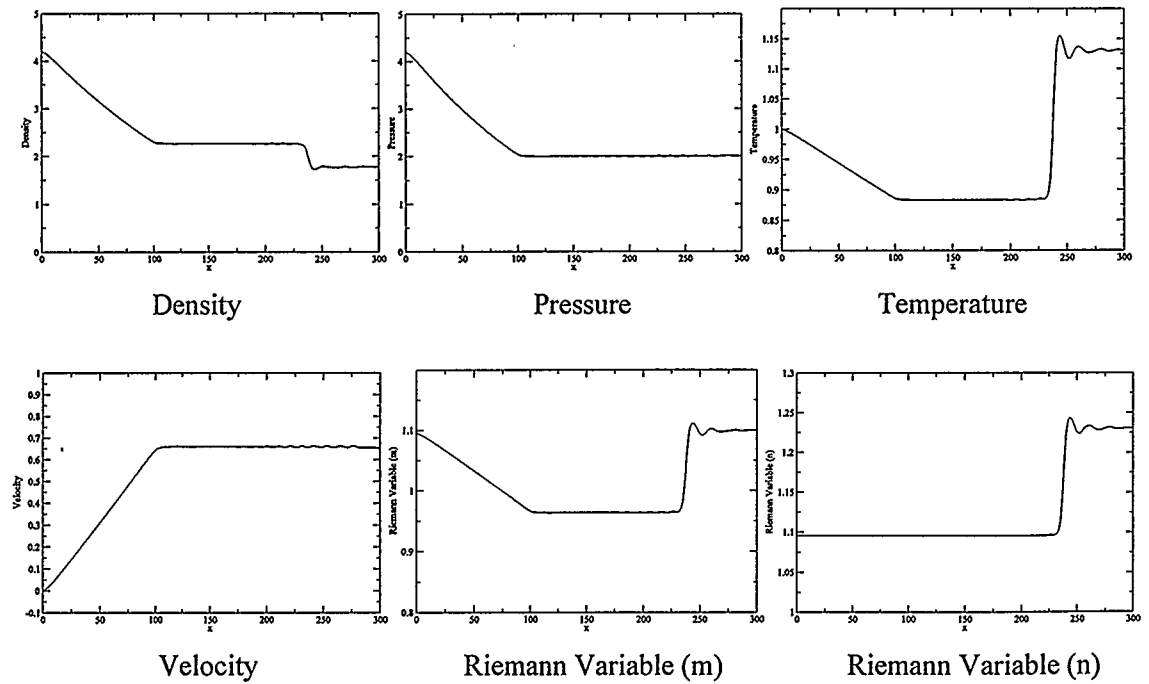


Fig. 5-2.4 Shock tube at time-step 1500

5-3 Reflection Validation By Relative Error at Shock Waves

For shock tubes, given the initial condition, including the high pressure p_4 (or the pressure p_2) and the low pressure p_1 , the exact solution consisting of the post-shock Mach number M and the shock pressure p_2 can be obtained from Eq. (5-2.1) and Eq. (5-2.2). A reflection is generated when an outgoing subsonic shock wave crosses a boundary, as demonstrated by Hedstrom. If there is no reflection, the pressure p_2 behind the shock should stay constant when the shock crosses the right boundary. So, a convenient measure of the reflection is the relative error in pressure after the shock has crossed the boundary, defined as:

$$\text{Relative error (\%)} = \frac{p_{num} - p_{an}}{p_{an}} \times 100 \quad (5-3.1)$$

Here, p_{num} is numerical pressure and p_{an} is the analytical pressure. (Thompson 1979).

To evaluate the relationship between relative error and domain lengths, as well as between the relative error and the shock Mach number, different domain lengths and different p_4 are selected while the grid $\Delta x = 0.02$ is maintained constant. The domain lengths are selected as 2, 4, 10, 20, and 40. So, the number of grid points are 100, 200, 500, 1000, and 2000 and the selected values of p_2/p_1 are listed in Table 5-3.1. Because there are no length or time scales in this problem, fixed grid size and varying domain lengths would be equivalent to maintaining the constant length and varying the resolution. So, this test is equivalent to maintaining the constant length, say 10, then, the resolutions are 0.1, 0.05, 0.02, 0.01, and 0.005. However, because the error is taken over a fixed number of grid points, this is not equivalent to a convergence study, which is presented in section 5-4.

Table 5-3.1: Relative errors at different Mach numbers

R P2/P1	P4/P1	Mach Number	RE (%) pts 100	RE (%) pts 200	RE (%) pts 500	RE (%) pts 1000	RE (%) pts 2000
1.3	1.70069	0.4705	0.00354	0.00308	0.00862	0.00723	0.0111
1.4	1.981006	0.534	0.014	0.0384	0.0535	0.0379	0.0557
1.6	2.616611	0.6337	0.068	0.019	0.157	0.165	0.157
1.8	3.35803	0.7116	0.120	0.351	0.355	0.330	0.382
2	4.212763	0.7758	0.024	0.453	0.486	0.498	0.549
2.2	5.188755	0.8307	0.145	0.183	0.595	0.565	0.571
2.4	6.294559	0.8787	0.210	0.292	0.585	0.555	0.574
2.6	7.539171	0.9214	0.146	0.166	0.523	0.560	0.54
2.8	8.932149	0.9599	0.695	0.278	0.526	0.374	0.486
3	10.48357	0.9951	0.867	0.375	0.458	0.363	0.414

Note: "pts" stands for grid points (over the domain length)

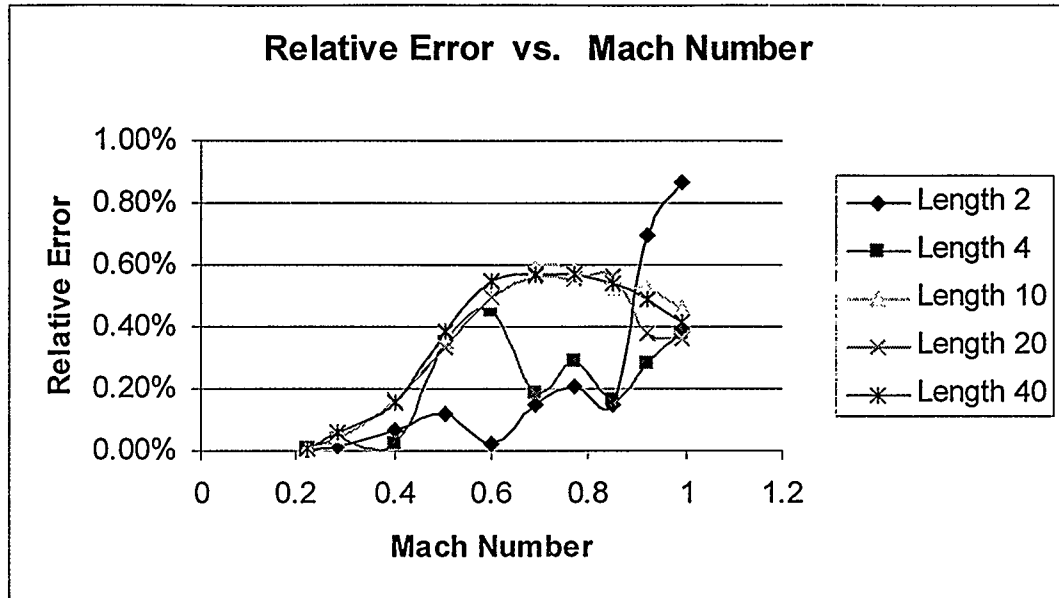


Fig. 5-3.1 Relative error vs. Mach number

From the results, one sees that with increasing Mach number, the reflection increases until the Mach number reaches 0.83 and then decreases when the Mach number is greater than 0.83 for domain lengths 10, 20 and 40. The worst case is at $M=0.83$ with a reflection of 0.595%. However, we could not get the same pattern for the domain length 2 and 4. Looking more closely at the perturbation of shock in shock tube for the short computational domain, it is found that the shock is not deep enough when the domain length is too short. So, we conclude that when the domain length is too short, the numerical simulation is not good enough to show shock conditions and the result. So, the results at domain length 2 and 4 do not show reflection pattern accurately.

Comparing with Thompson's result, in which the worst case of RE is 0.82% at $M=0.98$, one can see that the reflection is also related to the numerical scheme; for higher order schemes, the reflection is lower. Thompson used a first-order accuracy method in space and second-order accuracy method in time; and he found that the worst case was obtained at $M=0.98$ while in our case this occurs at $M=0.85$.

5-4 Reflection Validation Using the Riemann Variable

According to the discussion in section 4-3, for isentropic flow, the Riemann invariants are constant along their characteristic lines, Eqs. (4-3.3). Denoting the Riemann variables by m and n , where $m = c - \frac{\gamma-1}{2}u$ and $n = c + \frac{\gamma-1}{2}u$, then Eqs. (4-3.3) are equivalent to Eqs. (5-4.1):

$$\begin{cases} s = \text{const} \\ m = c - \frac{\gamma-1}{2}u = \text{const.} & \text{for } dx = (u - c)dt \\ n = c + \frac{\gamma-1}{2}u = \text{const.} & \text{for } dx = (u + c)dt \end{cases} \quad (5-4.1)$$

For the waves moving to left, the Riemann variable n is constant as follow (Kentfield 1993):

$$n = c + \left(\frac{\gamma-1}{2}\right)u = \text{const} = C \quad (5-4.2)$$

In this shock tube case, the constant value C at the left hand boundary is:

$$n = C = c + \left(\frac{\gamma-1}{2}\right)u = \sqrt{1.2 \frac{p_0}{\rho_0}} = 1.09544511501033$$

According to the analysis in section 4-3, the incoming Riemann variable should be constant if there is no reflection at the boundary. The fluctuation in the Riemann variable is a useful method to measure the reflections at the boundary and to verify accuracy. Because the analytical Riemann variable ($n = 1.09544511501033$) is very

close to 1, the absolute deviation between the numerical Riemann variable and the analytical Riemann variable is used to measure reflection instead of using a relative deviation (as above):

$$\text{Riemann Variable deviation} = | n_{num} - n_{an} |$$

Where n_{num} is the numerical Riemann variable and n_{an} is the analytical Riemann variable.

To analyze the relationship between Riemann variable deviations and the grid size when the expansion waves go through boundary, the reflection was evaluated on a fixed computational domain length, $L=10$, with variable number of grid cells, 100, 200, 300, 500, 700, 1000, and 2000 in the domain. Accordingly, the grid sizes were 0.1000, 0.0500, 0.0333, 0.0200, 0.0143, 0.0100, and 0.0050. The program was tested in single and double precision format, for reasons that will become obvious in view of the results below.

Table 5-4.1, Fig. 5-4.1 and Fig. 5-4.2 show the ten points average of the deviation between Riemann variables at the same, fixed, physical position for grid size 0.1000, 0.0500, 0.0333, 0.0200, 0.0143, 0.0100, and 0.0050 with the same domain length 10 and in single precision. Values shown are averaged over the ten grid points that surround the fixed physical location.

The Riemann variable deviation (RVD) should decrease with decreasing grid size (GS). In addition, the relationship should be $RVD = C(GS)^3$, where C is a constant number. Indeed, as indicated in Chapter 3, a fifth-order WENO scheme in space and a third-order Runge-Kutta method in time are used within the computational domain. Furthermore, at boundaries, a fourth-order one-sided scheme in space and second-order Runge-Kutta method in time are applied. So, we expect the Riemann variable deviation

to decrease while the grid size is reduced and that third-order accuracy will be obtained.

Table 5-4.1: Riemann variable deviation for different grid sizes (single precision)

No. of Grid Points	Grid Size	Deviation
100	0.1	2.30E-06
200	0.05	5E-07
300	0.033333333	7.23E-07
500	0.02	1.30799E-06
700	0.014285714	1.58E-06
1000	0.01	3.98E-06
2000	0.005	8.78499E-06

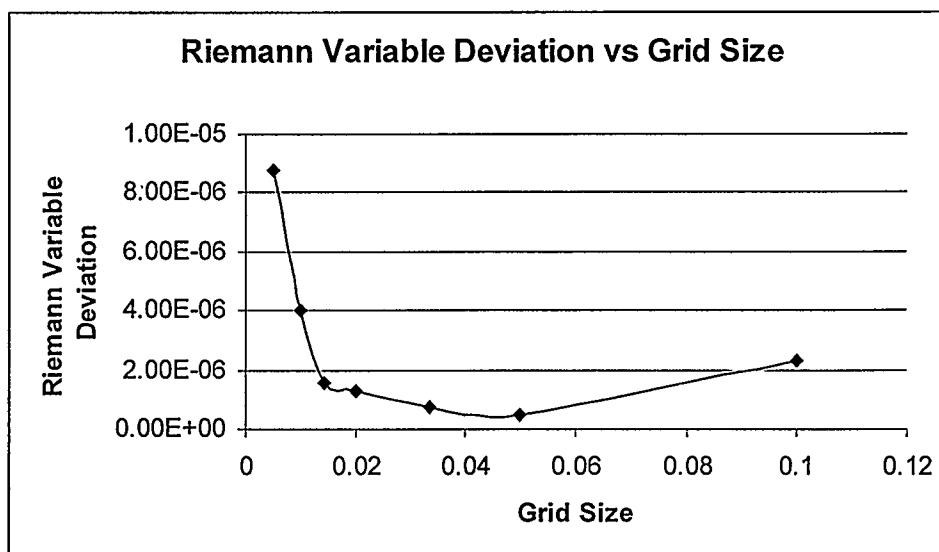


Fig. 5-4.1 Riemann variable deviation vs grid size (single precision)

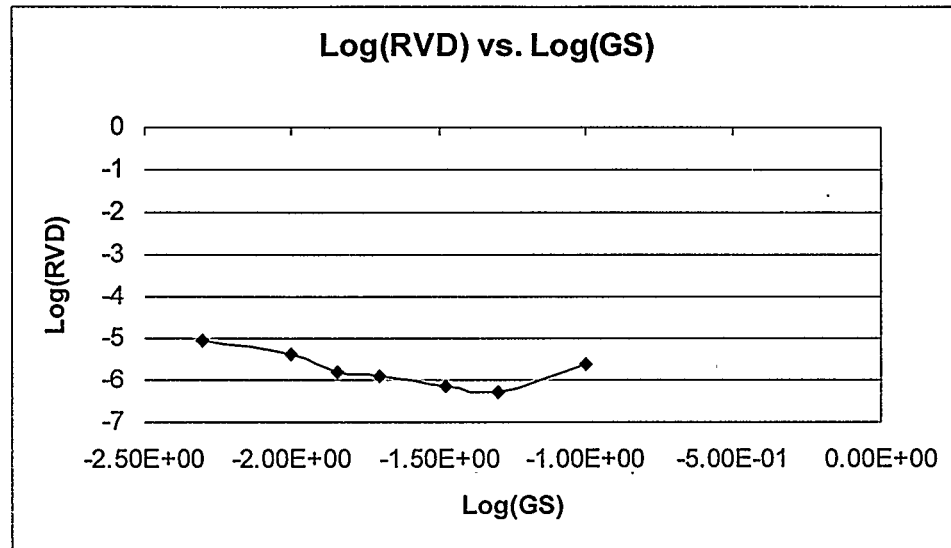


Fig. 5-4.2 Riemann variable deviation vs. grid size on a log-log scale (single precision)

In these single precision results, the Riemann variable deviation vs. grid size on a log-log scale is not proportional and the slope is off from 3 when the grid size is less than 0.05. Close examination of the data reveals that the Riemann variable deviations are less than 10^{-7} when the grid size is less than 0.05. This is consistent with numerical round-off errors due to the limited (four bytes) accuracy that becomes significant compared with the Riemann variable deviations, or even greater than the expected values of the Riemann variable deviation.

The same results as above but in double precision are shown in the table 5-4.2 and in Fig. 5-4.3 and Fig. 5-4.4.

Fig. 5-4.5 to Fig. 5-4.8 show the same relationship on a log-log scale at four physical positions. Fig. 5-4.4 plots the ten physical positions average of log (RVD) and log (GS) at these positions.

Table 5-4.2: Riemann variable deviation at different grid sizes (double precision)

No. of Grid Points	Grid Size	Deviation
100	0.1	1.85E-06
200	0.05	1.00594E-07
300	0.033333333	2.42E-08
500	0.02	8.89174E-09
700	0.014285714	2.89E-09
1000	0.01	1.39E-09
2000	0.005	1.033E-11

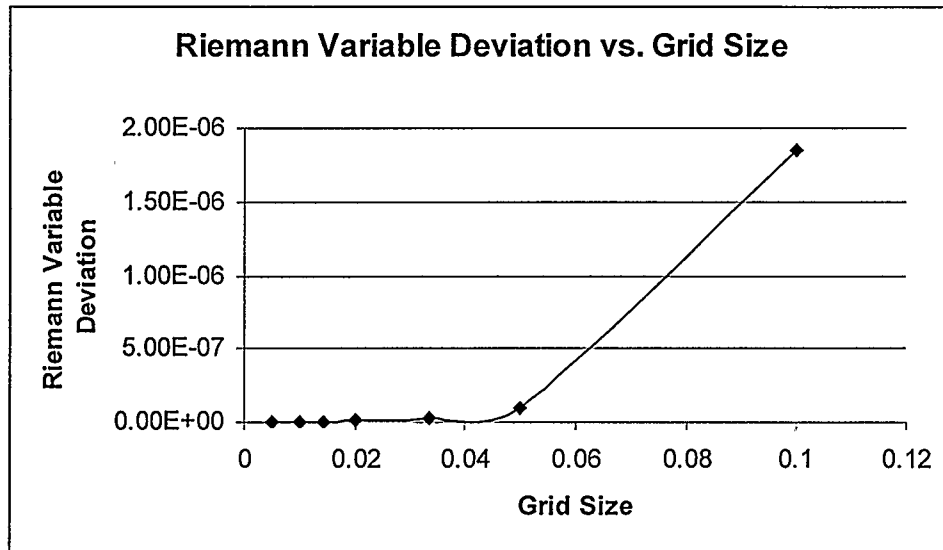


Fig. 5-4.3 Riemann variable deviation vs. grid size (double precision)

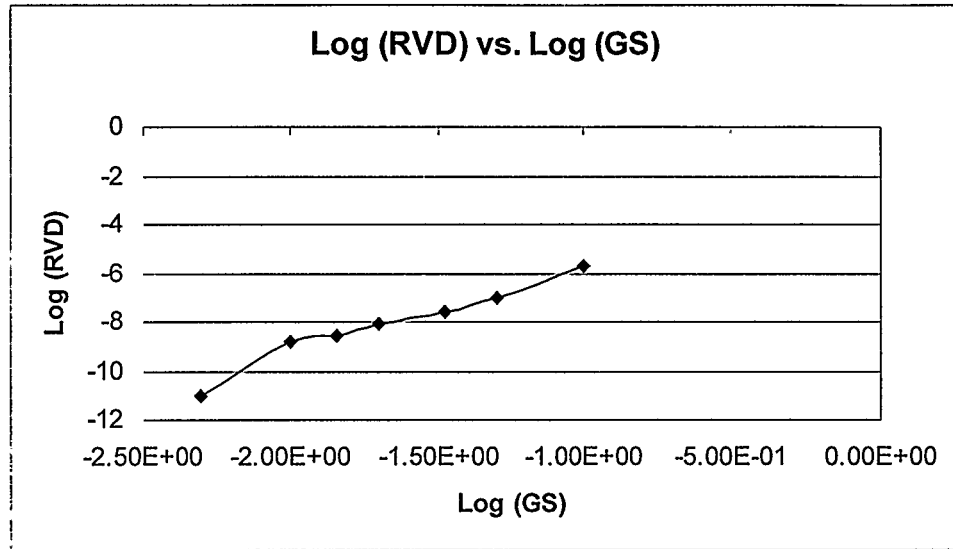


Fig. 5-4.4 Riemann variable deviation vs. grid size on a log-log scale (double precision)

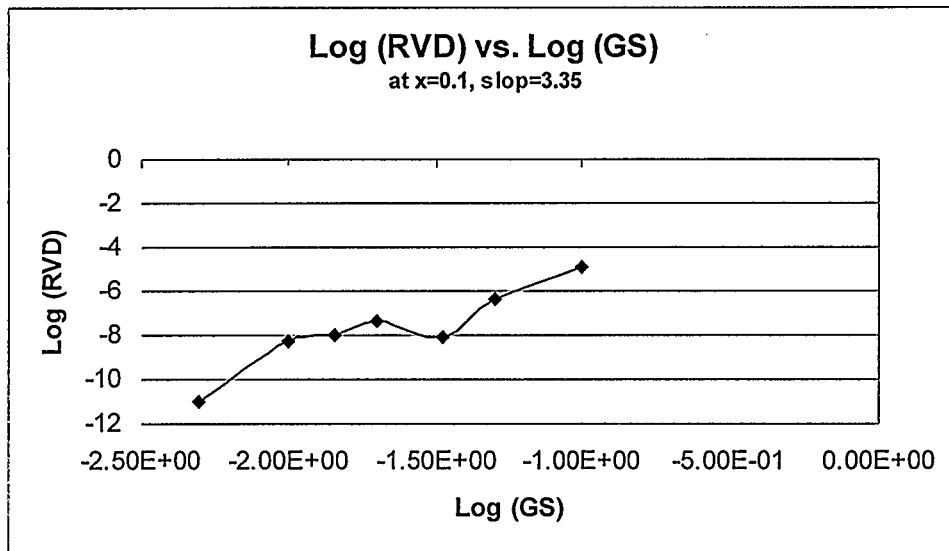


Fig. 5-4.5 Riemann variable deviation vs. grid size on a log-log scale at $x=0.1$ (double precision)

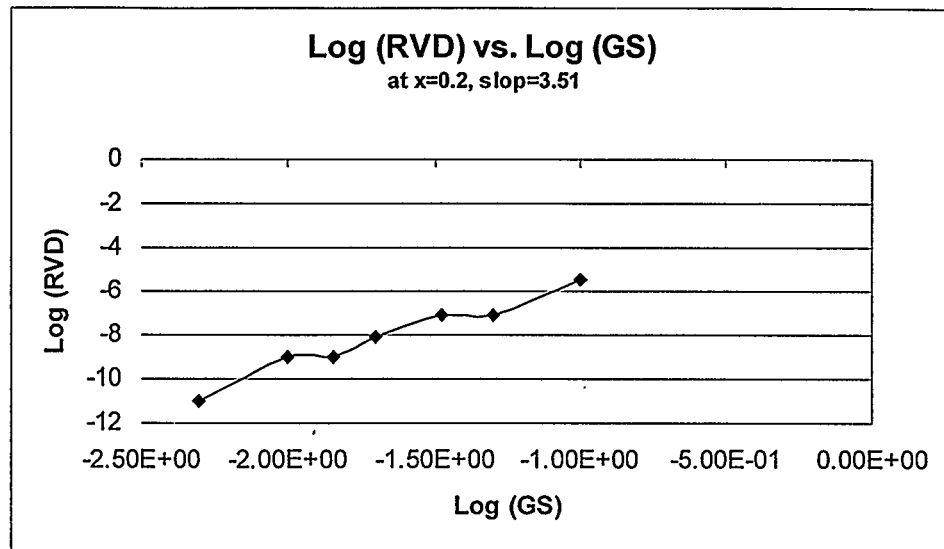


Fig. 5-4.6 Riemann variable deviation vs. grid size on a log-log scale at $x=0.2$ (double precision)

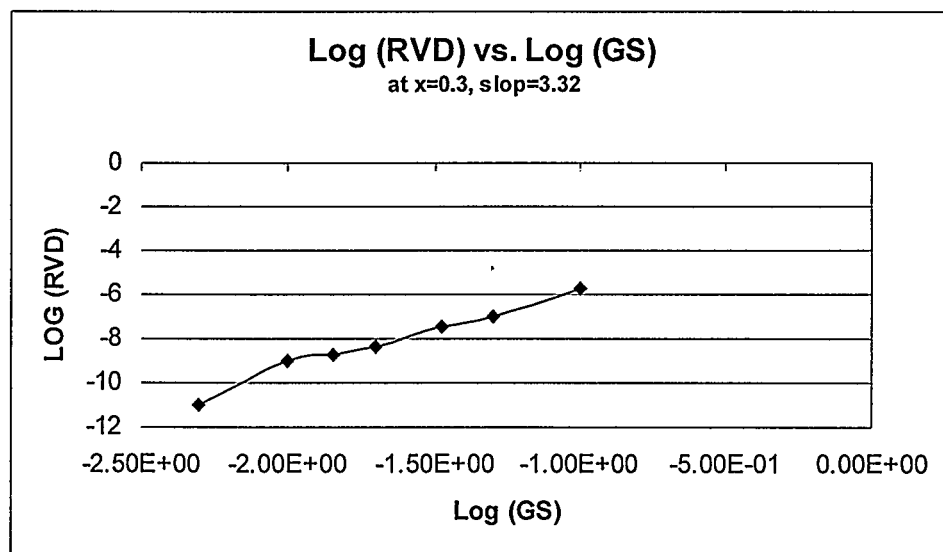


Fig. 5-4.7 Riemann variable deviation vs. grid size on a log-log scale at $x=0.3$ (double precision)

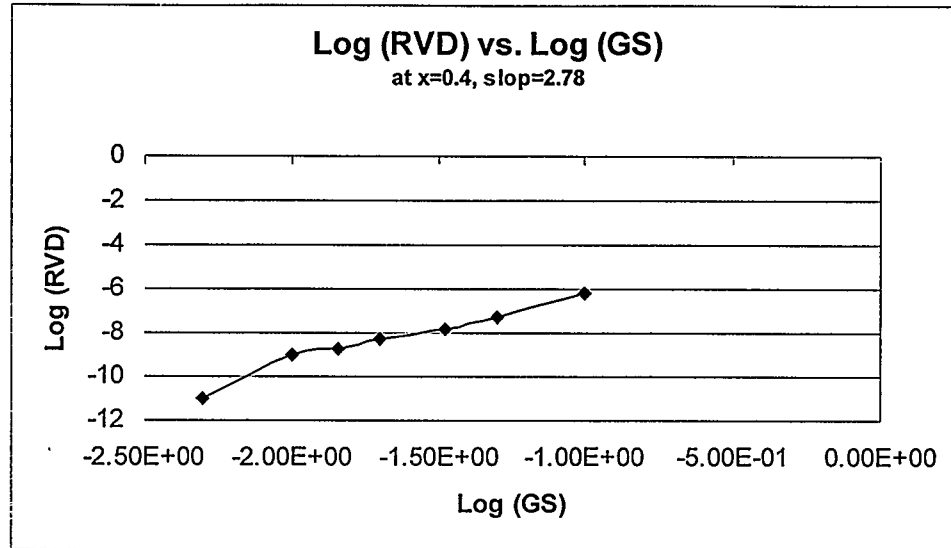


Fig. 5-4.8 Riemann variable deviation vs. grid size on a log-log scale at $x=0.4$ (double precision)

The results in Fig. 5-4.3 show a Riemann variable deviation decreasing when the grid sizes decrease, as expected, given the accuracy of the algorithm used. These results demonstrate that the code and boundary conditions as implemented are performing with the expected accuracy. In Fig. 5-4.4, the log-log plot is close to linear with a slope of approximately 4, which means that the overall accuracy of the scheme used is definitely of order 3. Moreover, this result also confirms that if the order of approximation near the boundary is equal to the scheme order minus one, the overall accuracy of the scheme used inside the domain is not affected (Poinsot et al. 1992).

5-5 Two-dimensional Validation

There are no analytical solutions available for two-dimensional, unsteady flow. Thus, one cannot by comparison validate numerical results with an exact solution. However, since the goal of the non-reflecting boundary condition is to simulate infinite computational domain, it is reasonable to compare smoke foils for computational domain of varying lengths.

Two different domain lengths ($30 L_{1/2}$ and $50 L_{1/2}$ respectively) were used, with the same domain width ($20 L_{1/2}$). Numerical smoke foils are shown on Fig. 5-5.1 and Fig. 5-5.2.

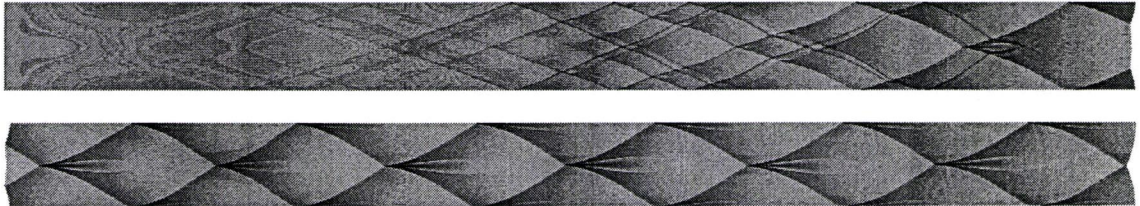


Fig 5-5.1 Smoke foils width: $20 L_{1/2}$, length: $30 L_{1/2}$

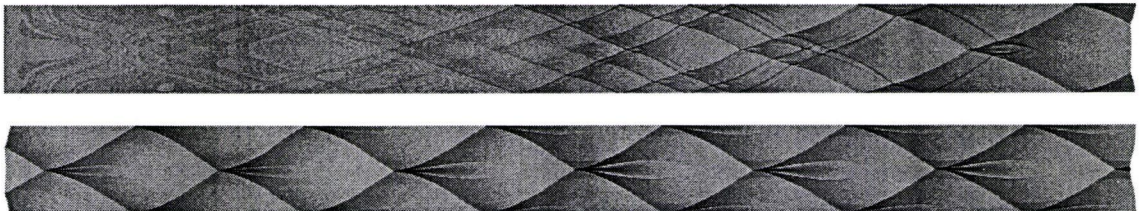


Fig 5-5.2 Smoke foils width: $20 L_{1/2}$, length: $50 L_{1/2}$

Comparing Fig. 5-5.1 and Fig. 5-5.2, one can see that domain lengths of $30 L_{1/2}$ and $50 L_{1/2}$ result in the same number of cells across the smoke foil.

DETONATION CELL SIZE

In this chapter, the non-reflecting boundary condition (BC) is used in a study of cell width and the comparison of smoke foils with non-reflecting BC and with the relaxation BC is performed.

6-1. Numerical Simulation

To demonstrate the relationship between domain width and cell size (or number of cells), computations were performed for the same set of parameters (see table 6-1.1) at different domain widths. Using the characteristic-based non-reflecting BC for the case described in table 6-1.1, the results are obtained and presented in figures below.

Table 6-1.1: Parameters

Overdrive (f)	Rate law (v)	Heat Release (Q)	Activation Energy (E_0)	Resolution (cells/ $L_{1/2}$)
1.2	0.5	50	10	32

To show the effect of the different boundary conditions, computations were also performed for the same set of parameters (see table 6-1.1) but using the relaxation boundary condition. The relaxation boundary condition attempts to relax the flow to the desired conditions at infinity. To that effect, at the boundary, the variables are set as:

$$\phi = (1 - \tau)\phi_{n\alpha,j,k} + \tau\phi$$

The results are presented in the following figures. The figures show numerically generated smoke foils.

As mentioned in Chapter 2, the structure of detonation fronts can be displayed on smoke foils not only experimentally but also numerically. There are different ways to generate numerical smoke foils. The method used here is based on the one discussed by Oran and Boris (1987) and used by Williams (2002). The leading shock is positioned by capturing the maximum flow acceleration along the propagation direction. The acceleration at each cell is calculated by the local pressure gradient divided by the average density, and the maximum acceleration is determined by using Eq. (6-1.1).

$$a_{\max} = \max(a_{i+1/2,j}) = \max\left(\frac{2(p_{i,j} - p_{i-1,j})}{(x_i - x_{i-1})(\rho_{i,j} + \rho_{i-1,j})}\right) \quad (6-1.1)$$

The smoke foil is then generated as a grayscale map of the leading shock pressure as a function of space and time in a frame of reference attached to the unburned fluid. This method clearly shows the triple point tracks. Its main drawback is that it does not show secondary structures within the reaction zone, behind the leading shock, see Williams (2002).

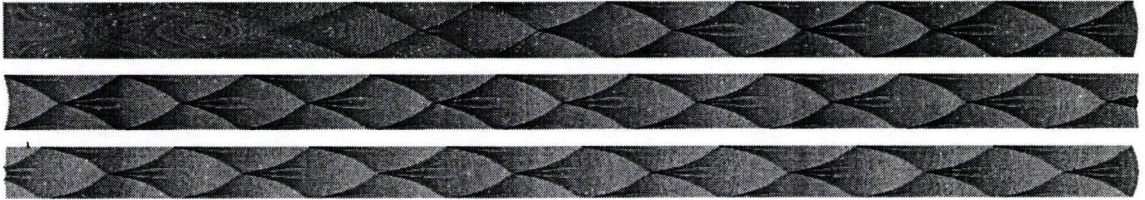


Fig. 6-1.1 Smoke foil width: $13 L_{1/2}$, length: $30 L_{1/2}$, Non-reflecting BC

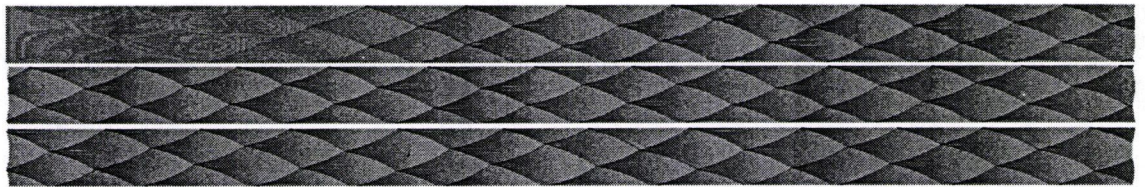


Fig. 6-1.2 Smoke foil width: $13 L_{1/2}$, length: $30 L_{1/2}$, relaxation BC

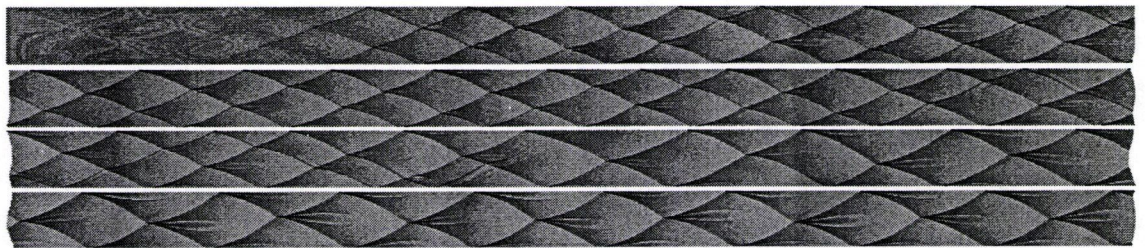


Fig. 6-1.3 Smoke foil width: $13 L_{1/2}$, length: $50 L_{1/2}$, relaxation BC

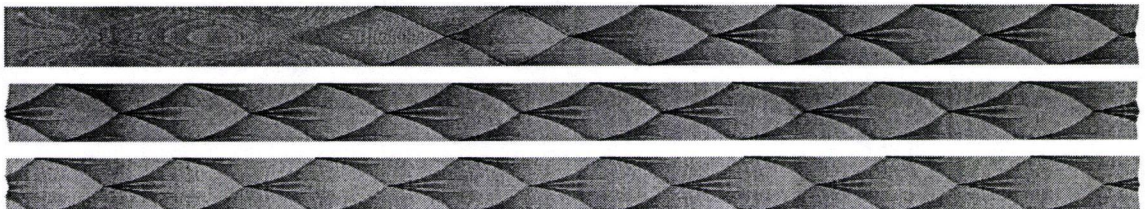


Fig. 6-1.4 Smoke foil width: $14 L_{1/2}$, length: $30 L_{1/2}$, Non-reflecting BC

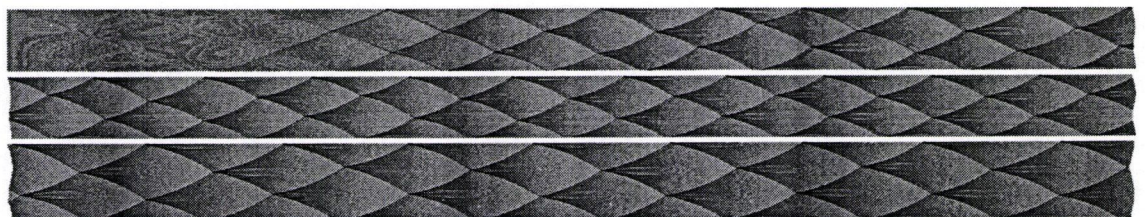


Fig. 6-1.5 Smoke foil width: $14 L_{1/2}$, length: $30 L_{1/2}$, relaxation BC

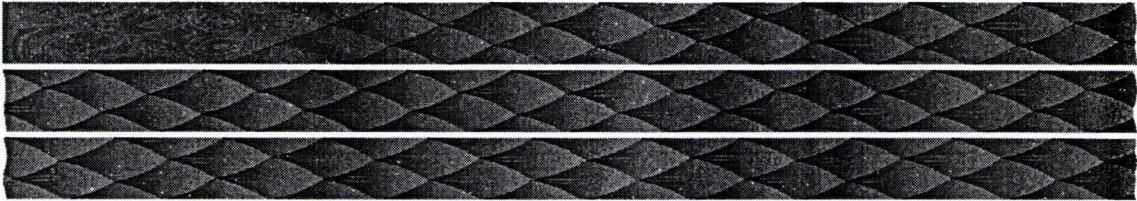


Fig. 6-1.6 Smoke foil width: $14 L_{1/2}$, length: $50 L_{1/2}$, relaxation BC

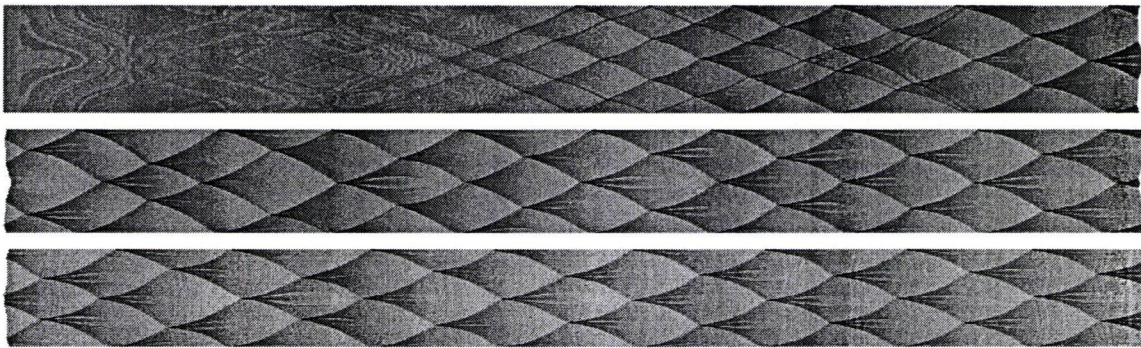


Fig. 6-1.7 Smoke foil width: $24 L_{1/2}$, length: $30 L_{1/2}$, Non-reflecting BC

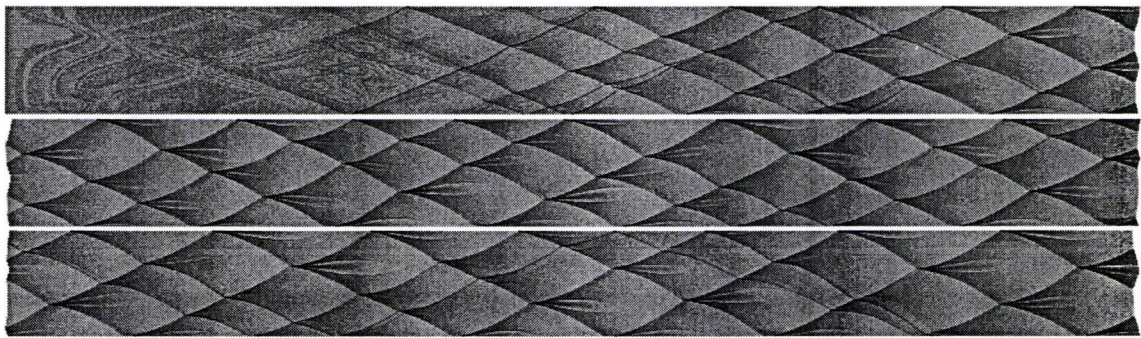


Fig. 6-1.8 Smoke foil width: $24 L_{1/2}$, length: $30 L_{1/2}$, relaxation BC

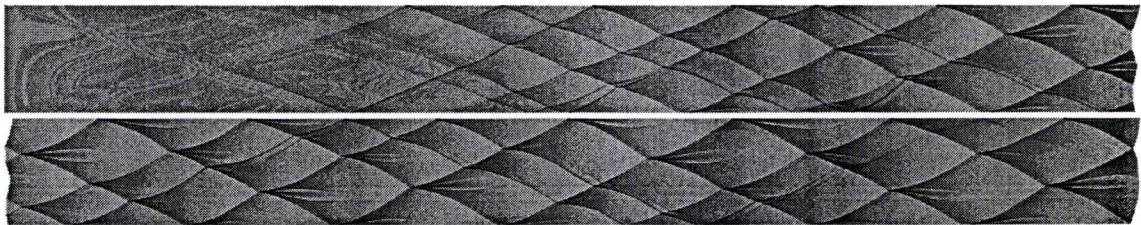


Fig. 6-1.9 Smoke foil width: $24 L_{1/2}$, length: $50 L_{1/2}$, relaxation BC

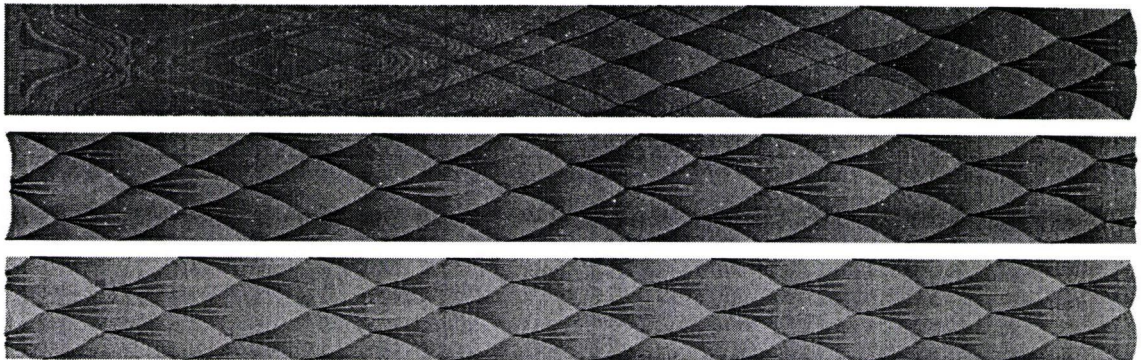


Fig. 6-1.10 Smoke foil width: $25 L_{1/2}$, length: $30 L_{1/2}$, Non-reflecting BC

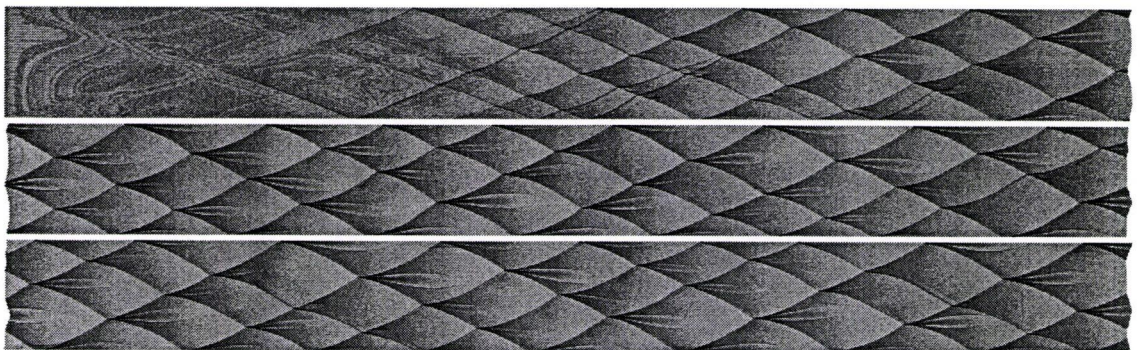


Fig. 6-1.11 Smoke foil width: $25 L_{1/2}$, length: $30 L_{1/2}$, relaxation BC

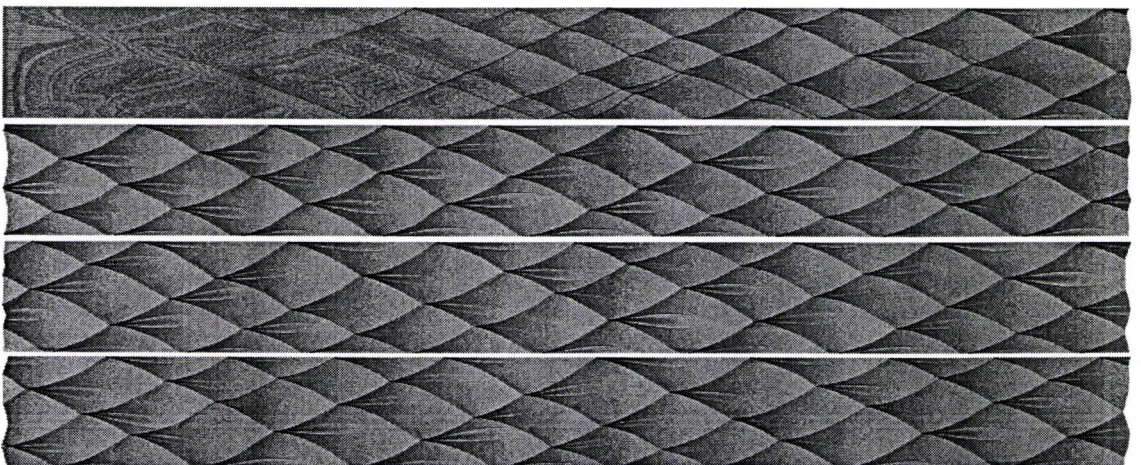


Fig. 6-1.12 Smoke foil width: $25 L_{1/2}$, length: $50 L_{1/2}$, relaxation BC

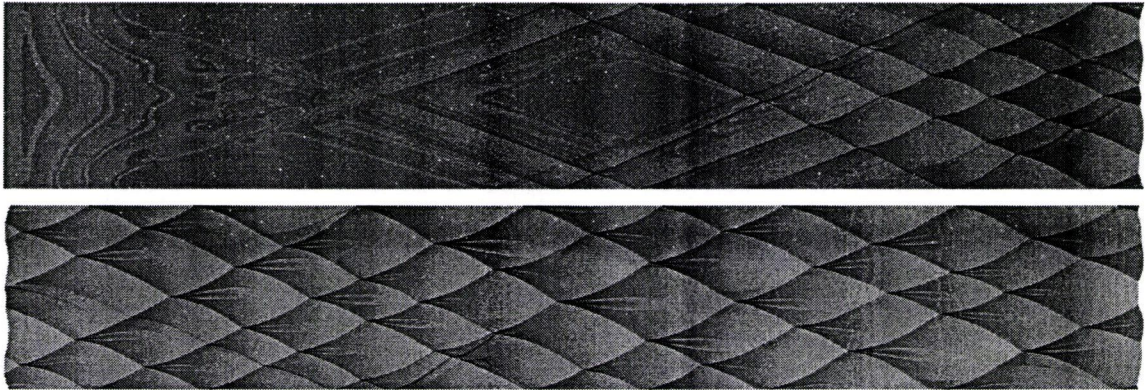


Fig. 6-1.13 Smoke foil width: $41 L_{1/2}$, length: $30 L_{1/2}$, Non-reflecting BC

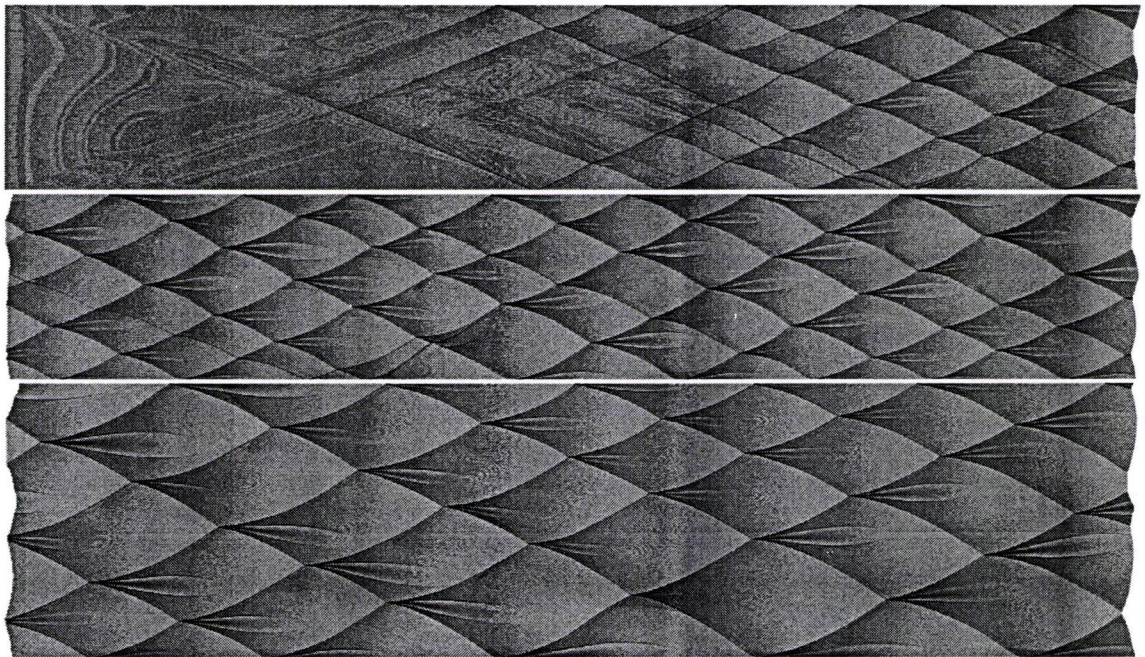


Fig. 6-1.14 Smoke foil width: $41 L_{1/2}$, length: $30 L_{1/2}$, relaxation BC

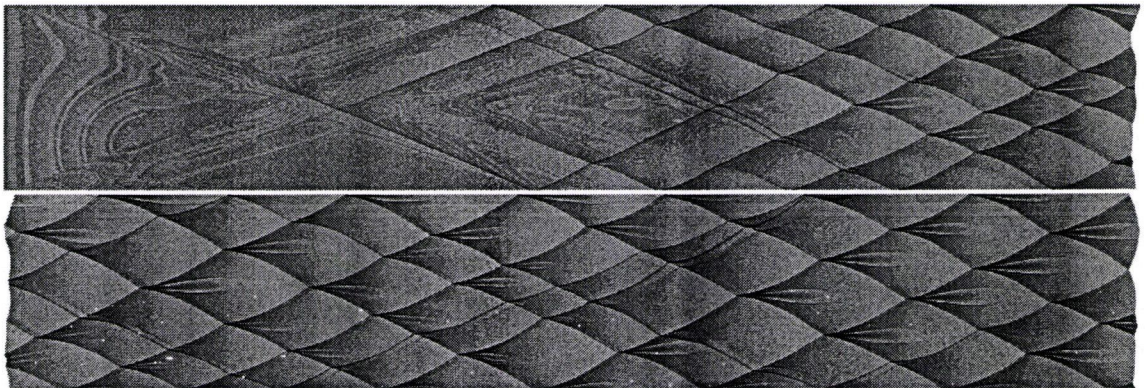


Fig. 6-1.15 Smoke foil width: $41 L_{1/2}$, length: $50 L_{1/2}$, relaxation BC

6-2. Comparison Between the Two Sets of Results

The comparison between two sets of numerical smoke foils is shown in table 6-2.1:

Table 6-2.1 The Comparison of smoke foils for different domain sizes and BC

Number of Figs.	Domain Size (Width X Length) (Number of $L_{1/2}$)	Boundary Condition	Number of Cells Across
6-1.1	13 X 30	Non-reflecting	1
6-1.2	13 X 30	Relaxation	1.5
6-1.3	13 X 50	Relaxation	1
6-1.4	14 X 30	Non-reflecting	1
6-1.5	14 X 30	Relaxation	1.5
6-1.6	14 X 50	Relaxation	1.5
6-1.7	24 X 30	Non-reflecting	2
6-1.8	24 X 30	Relaxation	1.5
6-1.9	24 X 50	Relaxation	1.5
6-1.10	25 X 30	Non-reflecting	2
6-1.11	25 X 30	Relaxation	2
6-1.12	25 X 50	Relaxation	2
6-1.13	41 X 30	Non-reflecting	3
6-1.14	41 X 30	Relaxation	3
6-1.15	41 X 50	Relaxation	3

From these results, one can conclude that:

- The number of cells across on the smoke foil (hence size) depends upon domain width. The wider the domain width, the more cells. There is only one cell formed for domain width $13 L_{1/2} \sim 20 L_{1/2}$, but the cell size becomes bigger with increasing domain width.

- Comparing Fig. 6-1.2 with Fig. 6-1.3, one can see that the cell numbers for domain length $30 L_{1/2}$ and $50 L_{1/2}$ are different and longer time is needed for cell formation and stabilization when the relaxation boundary condition is used. Comparing Fig. 6-1.1 with Fig. 6-1.3, one can see that the smoke foils are the same as the same cell numbers for domain length $30 L_{1/2}$ with non-reflecting BC and for $50 L_{1/2}$ with the relaxation BC.
- Comparing Fig. 6-1.10 with Fig. 6-1.11 and Fig. 6-1.12, one observes that the time for cell formation is shorter when the non-reflecting BC is applied than with relaxation BC.
- From Fig. 6-1.8, one can see that the number of cells changes from 2 to 1.5 with relaxation BC, when the domain length is $30 L_{1/2}$. When the domain is $50 L_{1/2}$, smoke foils with 1.5 cells across appear faster relatively and the cell number does not change (see Fig. 6-1.9).

CONCLUSION

A high order accurate Riemann variable-based non-reflecting boundary condition has been developed and incorporated into an ENO-based multidimensional reactive Euler solver. Validation was performed in three different ways.

- One-dimensional validation by using relative error on pressure in shock tube problems: The relative error at the outflow boundary was evaluated. The results show that the relative error is proportional to the shock velocity when the shock Mach number is less than 0.83; when the Mach number is greater than 0.83, the reflection decreases as the Mach number increases. The overall relative error is less than 0.6%

The relative error is also related to the numerical scheme. With a first-order accuracy numerical scheme, the relative error is less than 0.83%; with a third-order accuracy numerical scheme, the relative error is less than 0.6%.

- One-dimensional validation by using Riemann variable: The incoming Riemann variable at a fixed location close to the exit boundary was evaluated for decreasing grid sizes. Log-log plots of the Riemann variable deviation vs. grid size were found to be close to linear, with slope approximately equal to 4, showing an overall accuracy of the scheme at least equal to 3.

- Two-dimensional validation by comparing the different domain lengths of smoke foils: Since it is impossible to obtain exact solutions for two-dimensional, unsteady flow, the validation methods used for one-dimensional, unsteady flow can not be applied. It is also impossible to validate the result against experiments for two-dimensional simulations with simple chemical models, which are not a realistic representation of actual mixtures. The most feasible way to validate the reflecting is then to compare the numerical smoke foils for different domain lengths. For sufficient domain lengths, it is found that the same number of cells are obtained in a given domain width when the characteristics non-reflecting boundary condition is applied. When the relaxation boundary condition is used, the results for different domain lengths still result in different numbers of cells for these shorter domain lengths.

- Bauwens, L. & Williams, D. N. *Computation and Visualization of Detailed Detonation Structures*. Journal of AIAA 96-0343 (1996)
- Bauwens, L. *Ignition between a Shock and a Contact Surface – Influence of the Downstream Temperature*. Proceedings of the Combustion Institute 28, 653-661 (2000)
- Bauwens, L & Williams, D. N. *Three-Dimensional Detonation Cells* Journal of AIAA (2002)
- Bayliss, A. & Turkel, E. *Radiation boundary conditions for the wave-like equations* Commun. Pure Appl. Math. Vol.33, 708-725 (1980)
- Bayliss, A. & Turkel, E. *Far Field Boundary Conditions for Compressible Flows* Journal of computational Physics 48, 182-199 (1982)
- Berenger, J. P. *A Perfectly Matched Layer for the Absorption of Electromagnetic Waves* Journal of computational Physics Vol. 114, 185-200 (1994)
- Bourlioux, A. & Majda, A.J. *Theoretical and Numerical Structure for Unstable Two-Dimensional Detonations*. Combustion and Flame. 90 211-229 (1992)
- Chapman, D.L. *On the Rate of Explosion in Gases*. Philosophy Magazine 90-104 (1899)
- Colonius, S., Lele, K. and Moin, P. *Boundary condition for direct computation of aerodynamic sound generation* Journal of AIAA Vol. 31, 1574-1582 (1993)
- Courant, R., Friedrichs, K.O. & Lewy, H. *Über die partiellen Differenzgleichungen der mathematischen Physik*. Mathematische Annalen. 100,32-74 (German) (1928)

- Denisov, Yu. N. & Troshin, Ya. K. *Pulsating and Spinning Detonation of Gaseous Mixtures in Tubes*. Dokl. Akad. Nauk SSSR 125,110-113 (1959)
- Döring, W. *On Detonation Processes in Gases* Ann. Phys. 43, 421-436 (1943)
- Edwards, D.H., Hooper, G., Job, E.M. & Parry, D.J. *The behavior of the frontal and transverse shocks in gaseous detonation*. Astronautica Acta. 15 323-333 (1970)
- Engquist, B. and Majda, A. Math. Comput. Vol. 31, 629 (1977)
- Engquist, B. and Majda, A. Commun. Pure Appl. Math. 32, 312 (1979)
- Fickett, W. & Davis, W. C. *DETONATION* (1979)
- Giles, M. B. *Nonreflecting Boundary Conditions for Euler Equation Calculations* Journal of AIAA vol.28, No.12 2050-2058 (1990)
- Godunov, S.K. *A Difference Scheme for Numerical Computation of Discontinuous Solutions of the Hydrodynamic Equations*. Math Sbornik. 47, 271-306 (Russian) (1959)
- Jouguet, E. *On the Propagation of Chemical Reactions in Gases*. Journal of Pure and Applied Mathematics. 1,347-425 (1905)
- Kentfield, John A. C. *Nonsteady, One-Dimensional, Internal, Compressible Flows Theory and Applications* (1993)
- Hagstrom, T. and Hariharan S. I. *Accurate boundary conditions for exterior problems in gas dynamics* Math Computation, Vol.51, 581-597, (1988)

- Hedstrom, G. W. *Nonreflecting Boundary Conditions for Nonlinear Hyperbolic Systems* Journal of computational Physics 30, 222-237 (1979)
- Higdon, R. L. *Numerical Absorbing boundary conditions for wave equations* Math Computation, Vol.49, 65-90, (1987)
- Hirsch, C. *Numerical Computation of Internal and External Flows* Vol. 1 & Vol. 2. (1992)
- Hoffman, Joe D. *Numerical Methods for Engineers and Scientists* (2001)
- Hu, F. Q. *On Absorbing Boundary Conditions for Linearized Euler Equations by a Perfectly Matched Layer* Journal of computational Physics 129, 201-219 (1996)
- Hu, F. Q. *On Constructing Stable Perfectly Perfectly Matched Layer as an Absorbing Boundary Condition for Euler Equations* AIAA Journal (2002)
- Israeli M. and Orszag, S. *Approximation of Radiation Boundary Conditions* Journal of computational Physics 41, 115-135 (1981)
- Jiang, G. S. & Shu, C. W. *Efficient Implementation of Weighted ENO Schemes* Journal of Computational Physics 126, 202-228 (1996)
- Jiang, G. S. & Shu, C. W. *A High-Order WENO Finite Difference Scheme for the Equations of Ideal Magnetohydrodynamics* Journal of computational Physics 150, 561-594 (1999)
- John, James E. A. *Gas Dynamics* (1984)

- Jouguet, E. *On the Propagation of Chemical Reactions in Gases*. Journal of Pure and Applied Mathematics. 1, 347 -425 (1905)
- Laney, Culbert B. *Computational Gasdynamics* (1998)
- Lee, H. I. & Stewart, D. S. *Calculation of Linear Detonation Instability: One-Dimensional Instability of Plane Detonation* Journal of Fluid Mechanics. 216,103-132. (1990)
- Liu, Tai-Ping. *Shock Waves for Compressible Navier-Stokes Equations are Stable* Journal of Commun. Pure Appl. Math. 39, 565 (1986)
- Liu, X. D. sher, S. & Chan, T. *Weighted Essentially Non-oscillatory Schemes* Journal of Computational Physics 115, 200-212 (1994)
- Moen, I. O, J. W. Funk, S. A Ward, G. M. Rude & P. A. Thibault. *Detonation Length Scales for Fuel-Air Explosives*. Progress in Aeronautics and Astronautics. 94,55-79 (1985)
- Oran, E.S., Boris, J. P., Young, T., Flanigan, M., Burks, T.& Picone, M.. *Numerical Simulations of Detonations in Hydrogen-Air and Methane-Air Mixtures*. Proceedings of the Combustion Institute. 18,1641-1649 (1981)
- Oran, E.S., Young, T. R., Boris, J. P., Picone, M. & Edwards, D. H.. *A Study of Detonations Structure: The Formation of Unreacted Gas Pockets*. Proceedings of the Combustion Institute. 19,573-582 (1982)
- Oran, E.S., Boris, J. P. *Numerical Simulation of Reactive Flow*. Elsevier, New York. (1987)

- Poinsot, T. J. & Lele, S. K. *Boundary Conditions for Direct Simulations of Compressible Viscous Flows* Journal of Computational Physics 101, 104-129 (1992)
- Schott, G. L. *Observation of the Structure of Spinning Detonation.* Physics of Fluids 8, 850-865 (1965)
- Sharpe, G. J. *Transverse Waves in Numerical simulations of Cellular detonations* Journal of Fluid Mech. Vol.447, pp.31-51 (2001)
- Shu, C. W. & Osher, S. *Efficient Implementation of Essentially Non-oscillatory - Shock Capturing Schemes* Journal of Computational Physics 77, 439-471 (1988)
- Shu, C. W. & Osher, S. *Efficient Implementation of Essentially Non-oscillatory - Shock Capturing Schemes, II* Journal of computational Physics 83, 32-78 (1989)
- Sod, Gary A. *A Survey of Several Finite Difference Methods for Systems of Nonlinear Hyperbolic Conservation Laws* Journal of computational Physics 27, 1-31 (1978)
- Soloukhin, R.I. *Multiheaded structure of gaseous detonation.* Combustion and Flame. 9, 51-58 (1965)
- Streett, C. L. and Macaraeg, M. G. *Spectral Multi-domain for large-scale fluid dynamics simulations* Int. Journal Appl. Numer. Math. Vol. 6 123-139 (1989)
- Strehlow, R. A., Liaugminas, R., Watson, R. H. & Eyman, J. R. *Transverse Wave Structure in Detonations* Proceeding of the Combustion Institute 11, 683-692 (1967)
- Strehlow, R. A. *Multi-Dimensional Detonation Wave Structure. International Colloquium on Gasdynamics of Explosions* Novosibirsk, 24-29 August, 1969.

- Strehlow, R. A. *Combustion Fundamentals* (1984)
- Ta'asan and Nark, D. M. *An absorbing buffer zone technique for acoustic wave propagation* AIAA paper 95-0164 (1995)
- Taki, S. & Fujiwara, T. *Numerical Analysis of Two-Dimensional Nonsteady Detonations*. AIAA Journal. 16, 73-77 (1978)
- Taki, S. & Fujiwara, T. *Numerical Simulation of Triple Shock Behavior of Gaseous Detonation*. Proceedings of the Combustion Institute. 18, 1671-1681 (1981)
- Tam, C. K. W. and Webb, J. C. *Dispersion-Relation_Preserving schemes for computational acoustics* Journal of computational Physics 170, 262-281 (1993)
- Thompson, K. W. *Time Dependent Boundary Conditions for Hyperbolic Systems* Journal of Computational Physics 30, 222-237 (1979)
- Thompson, K. W. *Time-Dependent Boundary Conditions for Hyperbolic Systems, II*. Journal of computational Physics 89, 439-461 (1990)
- von Neumann, J. *Theory of Detonation Waves* John von Neumann, collected works, Vol.6, A.J. Taub. Macmillan, New York (1942)
- White, D. R. *Turbulent Structure of Gaseous Detonation*. Physics of Fluids. 4, 465-480 (1961)
- Williams, D. N. *Numerical Modeling of Detonations Near the Chapman-Jouguet Limit* (1995)
- Williams, D. N. *Numerical Modeling of Multidimensional Detonation Structure* (2002)

- Zel'dovich, Y. B. *On the Theory of the Propagation of Detonation in Gaseous Systems*
Journal of Experimental and Theoretical Physics 10, 542-568 (1940)